Tracing the cold and warm physico-chemical structure of deeply embedded protostars: IRAS 16293-2422 vs. VLA 1623-2417

Murillo Mejias, N.M.; Dishoeck, E.F. van; Wiel, M.H.D. van der; Jørgensen, J.K.; Drozdovskaya, M.N.; Calcutt, H.; Harsono, D.S.

Astronomy & Astrophysics manuscript no. IRAS_VLA_comparison_nmurillo_arxiv
May 15, 2018

Tracing the cold and warm physico-chemical structure of deeply embedded protostars: IRAS 16293-2422 versus VLA 1623-2417

N. M. Murillo[1], E. F. van Dishoeck[1,2], M. H. D. van der Wiel[3,4], J. K. Jørgensen[3], M. N. Drozdovskaya[1,5], H. Calcutt[3], and D. Harsono[1]

[1] Leiden Observatory, Leiden University, P.O. Box 9513, 2300 RA, Leiden, the Netherlands
e-mail: nmurillo@strw.leidenuniv.nl
[2] Max-Planck-Institut für extraterrestrische Physik, Giessenbachstraße 1, 85748, Garching bei München, Germany
[3] Centre for Star and Planet Formation, Niels Bohr Institute & Natural History Museum of Denmark, University of Copenhagen, Øster Voldgade 5–7, DK-1350 Copenhagen K., Denmark
[4] ASTRON, the Netherlands Institute for Radio Astronomy, Postbus 2, 7990 AA Dwingeloo, The Netherlands
[5] Center for Space and Habitability (CSH), University of Bern, Sidlerstrasse 5, CH-3012 Bern, Switzerland

May 15, 2018

ABSTRACT

Context. Much attention has been placed on the dust distribution in protostellar envelopes, but there are still many unanswered questions regarding the physico-chemical structure of the gas.
Aims. Our aim is to start identifying the factors that determine the chemical structure of protostellar regions, by studying and comparing low-mass embedded systems in key molecular tracers.
Methods. The cold and warm chemical structures of two embedded Class 0 systems, IRAS 16293-2422 and VLA 1623-2417 is characterized through interferometric observations. DCO^+, N_2H^+ and N_2D^+ are used to trace the spatial distribution and physics of the cold regions of the envelope, while c$-C_3H_2$ and C_2H from models of the chemistry are expected to trace the warm (UV-irradiated) regions.
Results. The two sources show a number of striking similarities and differences. DCO^+ consistently traces the cold material at the disk-envelope interface, where gas and dust temperatures are lowered due to disk shadowing. N_2H^+ and N_2D^+, also tracing cold gas, show low abundances towards VLA 1623−2417, but for IRAS 16293−2422, the distribution of N_2D^+ is consistent with the same chemical models that reproduce DCO^+. c$-C_3H_2$ and C_2H show different spatial distributions for the two systems. For IRAS 16293−2422, c$-C_3H_2$ traces the outflow cavity wall, while C_2H is found in the envelope material but not the outflow cavity wall. In contrast, toward VLA 1623−2417 both molecules trace the outflow cavity wall. Finally, hot core molecules are abundantly observed toward IRAS 16293−2422 but not toward VLA 1623−2417.
Conclusions. We identify temperature as one of the key factors in determining the chemical structure of protostars as seen in gaseous molecules. More luminous protostars, such as IRAS 16293-2422, will have chemical complexity out to larger distances than colder protostars, such as VLA 1623-2417. Additionally, disks in the embedded phase have a crucial role in controlling both the gas and dust temperature of the envelope, and consequently the chemical structure.

Key words. astrochemistry - stars: formation - stars: low-mass - ISM: individual objects: IRAS 16293-2422 and VLA1623-2417 - methods: observational - techniques: interferometric

1. Introduction

While there is a well-established outline of the physical evolution of protostellar systems (Evans 1999; Dunham et al. 2014; Li et al. 2014; Reipurth et al. 2014), there are still many questions regarding the physico-chemical structure of these systems. Several studies point out the chemical richness and diversity of young embedded protostars, most notably in the Class 0 stage, ranging from simple molecules to carbon chains and complex organics (see reviews by Herbst & van Dishoeck 2009; Caselli & Ceccarelli 2012; Sakai & Yamamoto 2013). In contrast, some other protostellar systems show much less chemical complexity (e.g., Jørgensen et al. 2005b; Maret et al. 2006; Öberg et al. 2014; Fayolle et al. 2015; Lindberg et al. 2014b, 2016, 2017; Bergner et al. 2017), a situation made more extreme when some starless cores have stronger molecular line emissions than the already formed protostars (e.g., Bergman et al. 2011; Bacmann et al. 2012; Friesen et al. 2014). It is interesting to explore the chemical structure and evolution of early stage protostars and what physical quantities dictate the resulting chemical structure as observed in the gas phase.

The chemical fingerprint generated in the early embedded stages of star formation may be transmitted to the later stages and eventually the protoplanetary disk, where planets and comets are formed (e.g., Aikawa et al. 1999; Aikawa & Herbst 1999; Visser et al. 2009, 2011; Hincelin et al. 2013; Drozdovskaya et al. 2014; Willacy et al. 2015; Yoneda et al. 2016). Which factors then generate a protostellar system's fingerprint? Protostellar cores may inherit their chemical composition from the parent clouds that eventually collapse to form protostars (e.g., Visser et al. 2009, 2011; Aikawa et al. 2012; Furuya et al. 2012; Tassis et al. 2012; Hincelin et al. 2016). It would then seem likely that protostars from the same parent cloud would have a similar chemical composition. However, this would require the cloud to have a homogeneous composition, which is not always the case (Bergman et al. 2011). Instead, other mechanisms could alter the chemi-

cal fingerprint. Turbulence and large-scale motions could stir the gas and dust of the cloud core around, moving material from the outer region of the core closer to the warmer regions of the system, kick-starting chemical reactions and producing enhancements of selected species. Formation of more complex chemical species likely occurs through grain-surface reactions (i.e., on ice and dust surfaces) instead of in the gas-phase, and such reactions proceed faster at higher dust temperatures which increases the mobility of radicals (Garrod & Herbst 2006). If material near outflow cavities is warmer than elsewhere in the envelope, this could generate pockets of chemically rich ices that, once heated above the sublimation temperature, would be released into the gas-phase (Drozdovskaya et al. 2015). Moreover, UV radiation can photodissociate CO and create free atomic carbon that leads to efficient formation of carbon-bearing molecules. UV irradiation together with age and variations in accretion rates would also produce different outcomes, even with the same initial ingredients. In addition, simple warm-chemistry molecules can be the precursors to more complex molecules (Sakai & Yamamoto 2013).

The physical evolution of the individual protostars, e.g., the collapse time and structure, will also impact the chemical fingerprint. An important consideration regarding the physical structure is that disks may have formed already in the early stages, as shown by recent observations (e.g., Tobin et al. 2012; Murillo et al. 2013; Harsono et al. 2014; Lindberg et al. 2014a; Codella et al. 2014; Yen et al. 2017). Not only do disks provide a high density long-lived reservoir preventing molecules from falling into the star, but they also affect the thermal structure of their surroundings. Thus the disk-envelope interface and the envelope itself must be studied (Murillo et al. 2015; Persson et al. 2016). The disk-envelope interface and the outer envelope of embedded systems are traced by cold-chemistry molecules, since these regions are usually shielded from heating by the central protostar (van Dishoeck et al. 1995; Jørgensen et al. 2004, 2005a; Sakai et al. 2014b; Murillo et al. 2015). Through the study of molecules sensitive to temperature, we can then understand the structure of embedded protostellar systems.

Aiming to explore the chemical evolution of the earliest embedded protostellar systems, i.e. Class 0, we compare two systems from ρ Ophiuchus ($d \sim 120$ pc, Loinard et al. 2008), IRAS 16293-2422 and VLA 1623-2417, separated by a projected distance of 2.8 pc. Most previous studies were based on single-dish studies. The advent of the Atacama Large Millimeter/submillimeter Array (ALMA) now allows chemical studies on 100 AU scales that spatially resolve the different physical components of the system.

IRAS 16293−2422 (hereafter IRAS 16293) is a widely studied multiple system, located in L1689N, with a complicated outflow structure being driven by source A (Stark et al. 2004; Yeh et al. 2008; Loinard et al. 2013; Kristensen et al. 2013; Girart et al. 2014). IRAS 16293 A and B, separated by about 620 AU, have different inclination angles, with A's disk-like structure being inclined and B orientated face-on with respect to the line of sight (Pineda et al. 2012; Jørgensen et al. 2016). Due to the different inclination angles, it is difficult to determine whether these systems are at the same evolutionary stage or not (Murillo et al. 2016). Both components are chemically rich but show differences in structure (Bottinelli et al. 2004; Bisschop et al. 2008; Jørgensen et al. 2011).

VLA 1623−2417 (hereafter VLA 1623) is a triple protostellar system, located in L1688 (ρ Oph A), mostly studied for its prominent outflow in the region (André et al. 1990; Caratti o Garatti et al. 2006). The three components of the system, VLA 1623 A, B and W are separated by 132 and 1200 AU, respectively, have similar inclination angles, and have also been found to be at different evolutionary stages (Murillo & Lai 2013; Murillo et al. 2013). VLA 1623 has been shown to be largely line poor in single-dish studies (Garay et al. 2002; Jørgensen et al. 2004; Bergman et al. 2011; Friesen et al. 2014).

In this paper, we present observations of DCO^+, N_2H^+, N_2D^+, c−C_3H_2 and C_2H towards IRAS 16293 and VLA 1623, using ALMA, the Submillimeter Array (SMA) and the Atacama Pathfinder EXperiment (APEX; Güsten et al. 2006). DCO^+, N_2H^+ and N_2D^+ are known to be good tracers of cold gas where CO is frozen out. c−C_3H_2 and C_2H are usually seen in photon-dominated regions (PDRs) such as the Orion Bar (Pety et al. 2007; van der Wiel et al. 2009; Nagy et al. 2015) and the Horsehead Nebula (Cuadrado et al. 2015; Guzmán et al. 2015), with both species located at the irradiated, and thus warmer, edge of these regions. c−C_3H_2 and C_2H could thus be expected to trace the (UV-irradiated) outflow cavity walls, although both species have also been found just outside the disk-envelope interface (Sakai et al. 2014a). Besides mapping their distributions, multiple lines from a single molecule can also be used to trace physical conditions such as temperature and density (van Dishoeck et al. 1993; Evans 1999; van der Tak et al. 2007; Shirley 2015) and the current dataset allows this to be done for several species.

Details of the observations with ALMA, SMA and APEX are described in Sect. 2. Section 3 describes the spatial distribution of each molecule for both systems. The observations are compared to chemical models and physical parameters are derived in Sect. 4. Sections 5 and 6 compare both systems studied here with other objects found in literature and place the results of our work in context.

2. Observations

2.1. IRAS 16293-2422

IRAS 16293 was targeted in the "Protostellar Interferometric Line Survey" (PILS) program (Project-ID: 2013.1.00278.S; PI: Jes K. Jørgensen; Jørgensen et al. 2016), an ALMA Cycle 2 unbiased spectral survey in Band 7, using both the 12m array and the Atacama Compact Array (ACA). The spectral set-up covers a frequency range from 329.147 GHz to 362.896 GHz, and provides a velocity resolution of 0.2 km s^{-1}. The phase center was α_{J2000} = 16:32:22.72; δ_{J2000} = −24:28:34.3, set to be equidistant from the two sources A and B at $v_{\rm lsr}$ = 3.1 and 2.7 km s^{-1} (Jørgensen et al. 2011), respectively. The resulting (u, v) coverage of the combined 12m array and the ACA observations are sensitive to the distribution of material with an extent of up to 13″ and a circular synthesized beam of 0.5″. A detailed description of the observations and reduction is given in Jørgensen et al. (2016). Many complex molecules detected in this survey (e.g., Coutens et al. 2016; Jørgensen et al. 2016; Lykke et al. 2017) show relatively compact emission peaking close to the location of the two protostars. This work focuses on a few of the molecules detected in the spectral survey that show extended emission, namely DCO^+, c−C_3H_2 and C_2H. Several transitions of c−C_3H_2 are present throughout the frequency range of PILS, however for this work, only a five transitions with strong observed emission were chosen in the 349 to 352 GHz frequency range. For all molecules the combined 12m array and ACA data cubes are used. The typical RMS noise is about 7–10 mJy beam^{-1} per 0.2 km s^{-1} channel, and the flux calibration uncertainty is ∼5% (Jørgensen et al. 2016). Transitions and line frequencies of the molecular species used in this work are listed in Table 1, as well

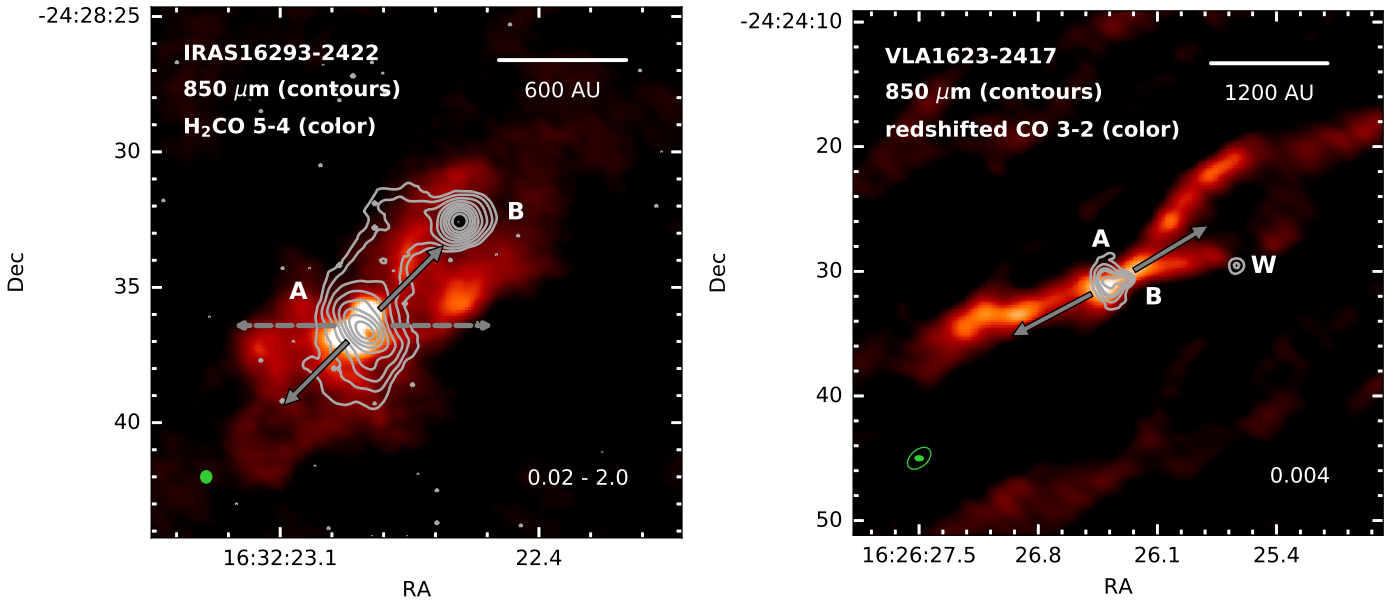

Fig. 1. Continuum at 850μm (contours) for both systems, IRAS 16293−2422 (left) and VLA 1623−2417 (right), overlaid on intensity integrated H_2CO (0 to 60 km s^{-1}; color-scale) and redshifted CO (4 to 15 km s^{-1}; color-scale), respectively. The green ellipses on the bottom left indicate the beam of the observations. For the right panel, the empty ellipse is the beam of the CO observations. For VLA 1623−2417, contours are in steps of 3, 8, 15, 20 and 50σ, with σ = 0.004 Jy beam^{-1}. For IRAS 16293−2422, the levels are logarithmically spaced between 0.02 and 2 Jy beam^{-1}, and highlight the ridge that spans between sources A and B. The arrows show the direction of red- and blue-shifted outflows from source A in each system.

as the peak intensities and line widths. Table A.1 lists further details of the observations, such as UV-baseline range and largest angular scale recovered in the observations.

Since the PILS survey did not cover lines of N_2D^+ 3–2 or DCO^+ 3–2, we include here the observations of these two molecules from a spectral line survey with the SMA (Jørgensen et al. 2011). The phase center was α_{J2000} = 16:32:22.91; δ_{J2000} = −24:28:35.5. For DCO^+ 3–2, the beam size is 5.5″×3.2″ (P.A. = 17.7°), while for N_2D^+ 3–2 the beam size is 4.0″×2.4″ (P.A. = −1.0°). The RMS noise is 0.24 Jy beam^{-1} for a 0.56 km s^{-1} channel width for DCO^+, and 0.06 Jy beam^{-1} for a channel width of 1.1 km s^{-1} for N_2D^+. Further details on the reduction and analysis are given in Jørgensen et al. (2011). These data are considered in order to directly compare the cold chemistry of IRAS 16293 with that of VLA 1623. Additionally, two transitions of DCO^+ are needed to derive temperature and density from line ratios.

2.2. VLA 1623-2417

VLA 1623 was observed with ALMA in Cycle 0 using Band 6, with phase center α_{J2000} = 16:26:26.419; δ_{J2000} = −24:24:29.988. The spectral set-up was configured to observe DCO^+ 3–2 and N_2D^+ 3–2 together with $C^{18}O$ 2–1 and ^{12}CO 2–1, providing a velocity resolution of 0.0847 km s^{-1} and a synthesized beam size of 0.85″×0.56″ (P.A. = −83.8°). DCO^+ 3–2 data from the Cycle 0 observations were previously presented in Murillo et al. (2015) and are added to this work for completeness in the comparison of both systems. The data reduction results of $C^{18}O$ and ^{12}CO can be found in Murillo et al. (2013) and Santangelo et al. (2015).

ALMA Cycle 2 observations of VLA 1623 were carried out in Band 6 and 7, with phase center α_{J2000} = 16:26:26.390; δ_{J2000} = −24:24:30.688. Baseline and frequency ranges are listed in Table A.1.

The Cycle 2 Band 6 spectral set-up covered DCO^+ 3–2, $C^{18}O$ 3–2, ^{13}CO 3–2 and c−C_3H_2 $6_{0,6}$–$5_{1,5}$ together with continuum. Data calibration was done with J1733-1304 and J1517-2422 for bandpass, J1625-2527 for gain calibration, and J1517-243, J1733-130, Ceres, Mars, and Titan were observed for flux calibration. The spectral windows with line emission have bandwidths of 62 MHz each, while for continuum the total bandwidth is of 8 GHz. These observations were carried out with both the Total power, ACA and 12m arrays, for a total of four configurations. With the 12m array, two configurations, C35-5 (25 ∼ 1000 m) and C34-1 (10 ∼ 350 m), were used in order to bridge the gap between the 12m and ACA array observations. Cycle 2 Band 6 ACA observations of DCO^+ were presented in Murillo et al. (2015) and are only included here for visual comparison. The 12m and ACA $C^{18}O$ and ^{13}CO observations from Cycle 2 Band 6 will be treated in a future publication. In this work, we focus only on the 12m array c−C_3H_2 $6_{0,6}$–$5_{1,5}$ observations from Cycle 2 Band 6 data. The C35-5 configuration provides an angular and velocity resolution of 0.45″×0.25″ (P.A. = 86.3°) and 0.0208 km s^{-1}, respectively, with a typical RMS noise of 7 mJy beam^{-1}. The C34-1 configuration results in an angular resolution of 1.60″×0.88″ (P.A. = 83.8°) with a channel width of 0.0208 km s^{-1} and a typical RMS noise of 20 mJy beam^{-1}.

Band 7 observations, with a spectral set-up covering N_2H^+ 5–4, DCO^+ 5–4 and H_2D^+ $1_{1,0}$–$1_{1,1}$ as well as continuum with only the 12m array, provided a spectral and angular resolution of 0.025 km s^{-1} and 0.88″×0.56″ (P.A. = −86.6°), respectively. The spectral windows with line emission have a total bandwidth of 62 MHz each, and continuum has a total bandwidth of 4 GHz. Total observing time was 0.9 hr with a 46% duty cycle, using 34 antennas and a maximum baseline of 350 m. Data calibration was done with J1517-2422, J1625-2527 and Titan for bandpass, gain and flux calibration, respectively. DCO^+ was detected with

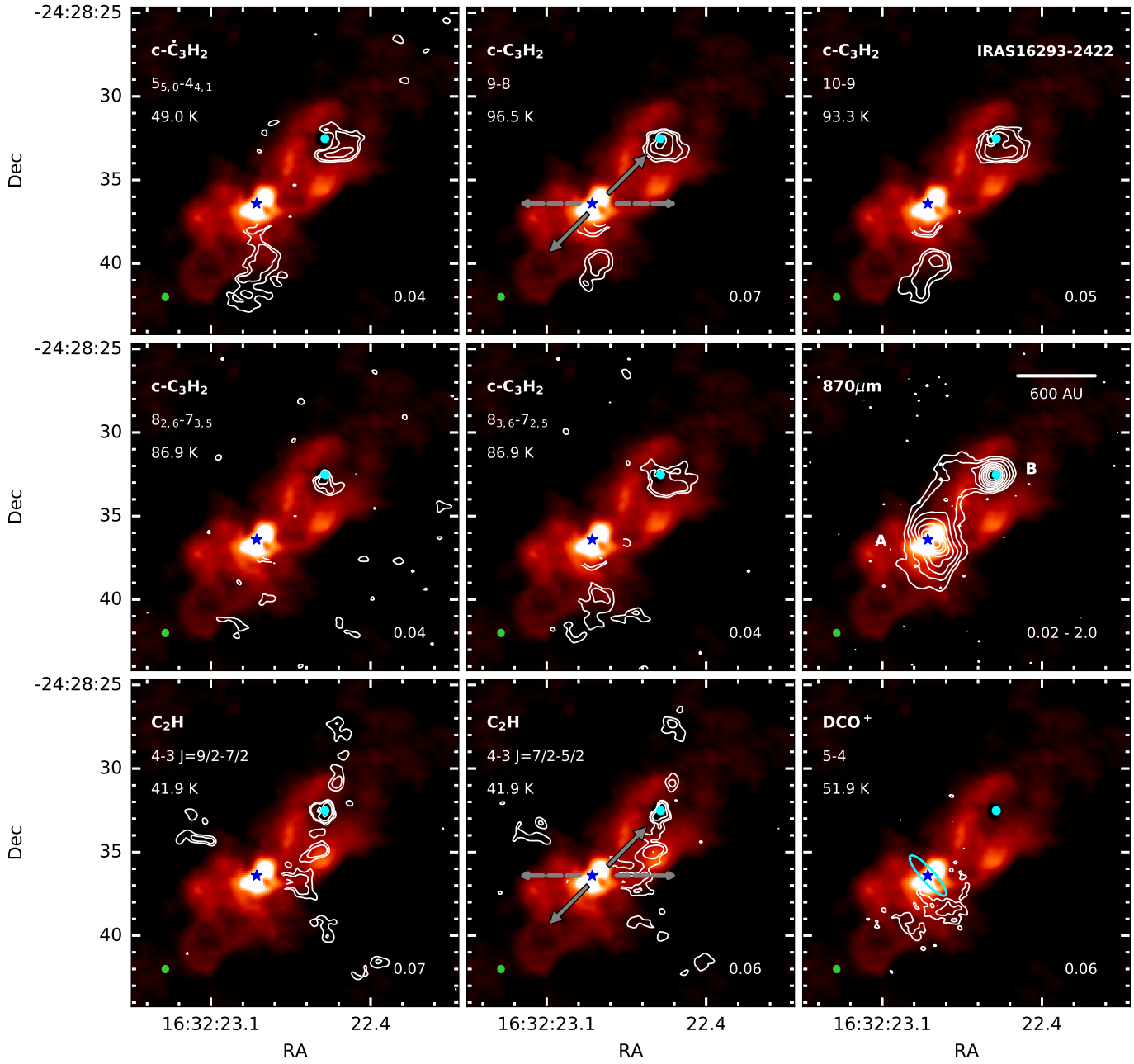

Fig. 2. Intensity integrated maps (contours) of c–C_3H_2, C_2H, DCO^+ and continuum towards IRAS 16293-2422. Intensity integrated H_2CO 5–4 (0 to 60 km s^{-1}) is shown in color-scale. Contours show the respective lines in steps of 2, 3, 5, 20 and 60σ, with σ (Jy $beam^{-1}$ km s^{-1}) indicated in the lower right of each panel. For continuum, the levels are logarithmically spaced between 0.02 and 2 Jy $beam^{-1}$, and highlight the ridge that spans between sources A and B. The positions of IRAS 16293-2422 A and B are indicated with a star and circle, respectively. The gray arrows indicate the outflow directions, while the cyan ellipse shows the disk-like structure. The green circle on the bottom left indicates the beam of the combined 12m and ACA observations. For the c–C_3H_2 and C_2H panels, the emission centered on A is contamination from other molecule(s) and is masked out in a radius of 2″ from the position of A.

a noise of 26 mJy $beam^{-1}$ per 0.025 km s^{-1}. The system temperature was relatively high for the spectral windows containing N_2H^+ and H_2D^+, causing the noise to be of about 95 mJy $beam^{-1}$ per 0.025 km s^{-1} velocity channel, despite flagging the antennas with the highest system temperature.

In this work we focus on the DCO^+ 3–2 and N_2D^+ 3–2 lines from the Cycle 0 12m array obsevations, in addition to c–C_3H_2 $6_{0,6}$–$5_{1,5}$, DCO^+ 5–4, N_2H^+ 5–4 and H_2D^+ $1_{1,0}$–$1_{1,1}$ 12m array observations from Cycle 2. Line transitions and frequencies together with peak intensities and line widths are listed in Table 1.

Additionally, single-dish APEX observations in the ON/OFF mode were carried out on 22 and 24 October 2016 using the heterodyne instrument SheFI (Belitsky et al. 2006; Vassilev et al. 2008) with Bands APEX-1 (213 – 275 GHz) and APEX-2 (267 – 378 GHz), targeting DCO^+ 3–2 and 5–4, as well as C_2H 4–3. These observations were taken to compare the location of C_2H in both VLA 1623 and IRAS 16293, as well as to have a separate verification and comparison of the physical parameters derived from ALMA observations and single-dish. Several transitions of NO and HCN were detected, both of which can form in gas and

Table 1. Summary of line observations.

					IRAS 16293-2422		VLA 1623-2417	
Line	Transition	ν	$\log_{10} A_{ij}$	E_{up}	Peak Intensity	Line width	Peak Intensity	Line width
		GHz		K	mJy beam^{-1}	km s^{-1}	mJy beam^{-1}	km s^{-1}
				ALMA				
c$-C_3H_2$	$6_{0,6}$–$5_{1,5}$	217.822148	-3.23	38.61	...	...	194	0.5
c$-C_3H_2$	$5_{5,0}$–$4_{4,1}$	349.26400	-2.78	48.98	240[a]	0.5	...	...
c$-C_3H_2$	10–9[b]	351.78158	-2.61	96.49	410[a]	0.6	...	...
c$-C_3H_2$	9–8[c]	351.96597	-2.67	93.34	350[a]	0.6	...	...
c$-C_3H_2$	$8_{2,6}$–$7_{3,5}$	352.18554	-2.76	86.93	90[a]	0.6	...	...
c$-C_3H_2$	$8_{3,6}$–$7_{2,5}$	352.19364	-2.76	86.93	200[a]	0.6	...	...
C_2H	4–3 J=9/2–7/2 F=5–4	349.33771	-3.88	41.91	170	0.6	...	...
C_2H	4–3 J=9/2–7/2 F=4–3	349.33899	-3.89	41.91	140	0.6	...	...
C_2H	4–3 J=7/2–5/2 F=4–3	349.39927	-3.90	41.93	140	0.6	...	...
C_2H	4–3 J=7/2–5/2 F=3–2	349.40067	-3.92	41.93	110	0.6	...	...
DCO^+	3–2	216.11258	-2.62	20.74	...	...	90	0.7
DCO^+	5–4	360.16978	-2.42	51.86	10	1.0	290	0.7
N_2D^+	3–2	231.32166	-2.66	22.20	...	...	<8.58[d]	...
N_2H^+	4–3	372.67251	-2.51	44.71	...	...	<94.9[d]	...
				SMA				
DCO^+	3–2	216.11258	-2.62	20.74	1800	1.0	...	...
N_2D^+	3–2	231.32166	-2.66	22.20	1700	2.0	...	...
				APEX (T_{mb})				
C_2H	4–3 J=9/2–7/2 F=5–4	349.33771	-3.88	41.91	...	...	0.96 K	0.7
C_2H	4–3 J=9/2–7/2 F=4–3	349.33899	-3.89	41.91	...	...	0.62 K	0.7
C_2H	4–3 J=7/2–5/2 F=4–3	349.39927	-3.90	41.93	...	...	0.68 K	0.7
C_2H	4–3 J=7/2–5/2 F=3–2	349.40067	-3.92	41.93	...	...	0.34 K	0.7
DCO^+	3–2	216.11258	-2.62	20.74	...	...	4.8 K	0.8
DCO^+	5–4	360.16978	-2.42	51.86	...	...	2.2 K	0.8

Notes. [a] c$-C_3H_2$ peak intensities and line widths taken from the south peak where there is no line confusion. [b] Blended $10_{0,10}$–$9_{1,9}$ and $10_{1,10}$–$9_{0,9}$ transitions of c$-C_3H_2$. [c] Blended $9_{1,8}$–$8_{2,7}$ and $9_{2,8}$–$8_{1,7}$ transitions of c$-C_3H_2$. [d] 1 σ noise level of N_2D^+ and N_2H^+ in 0.02 km s^{-1} channel

References. All rest frequencies were taken from the Cologne Database for Molecular Spectroscopy (CDMS) (Endres et al. 2016). The c$-C_3H_2$ entry was based on Bogey et al. (1987) with transition frequencies important for our survey from Bogey et al. (1986) and from Spezzano et al. (2012). The CCH entry is based on Padovani et al. (2009) with additional important data from Müller et al. (2000) and Sastry et al. (1981). The DCO^+ and N_2H^+ entries are based on Caselli & Dore (2005) and on Cazzoli et al. (2012), respectively. Information on the N_2D^+ rest frequency was taken from Pagani et al. (2009a).

surface reactions, whereas N_2H^+ and N_2D^+ only form in the gas. NO and HCN are not further analyzed in this work. The observations were centered on VLA 1623 A (α_{J2000} = 16:26:26.390; δ_{J2000} = −24:24:30.688). The typical RMS noise was 100 mK for APEX-1 and between 50 – 80 mK for APEX-2 in 0.1 km s^{-1} channels. Peak temperatures (T_{mb}) and line widths for Gaussian fits to the single dish lines are listed in Table 1. The typical calibration uncertainties are about 10% for the APEX SheFI instruments in the 230 and 345 GHz Bands. For APEX-1 and APEX-2 observations the HPBW is 28.7″ and 18″, respectively. The main beam efficiencies used are η_{mb} = 0.75 at 230 GHz, and η_{mb} = 0.73 at 345 GHz.

3. Results

3.1. IRAS 16293-2422

The molecules c$-C_3H_2$, C_2H and DCO^+ from the PILS spectral survey (Jørgensen et al. 2016) are considered here, together with DCO^+ and N_2D^+ from the SMA spectral survey (Jørgensen et al. 2011). The PILS survey images are obtained from the combined 12m array and ACA, which picks up the small and large scale emission from scales less than 13″. The peak intensities and widths of each line are listed in Table 1. Intensity integrated maps of each line overlaid on H_2CO are shown in Fig. 2. H_2CO $5_{1,5}$–$4_{1,4}$ from the PILS survey (van der Wiel et al. in prep.) is used as a reference for the more extended envelope and one of the outflow directions. The nominal velocities at which most species emit at source A and B are V_{LSR} =3.2 and 2.7 km s^{-1}. c$-C_3H_2$ and C_2H spectra at selected positions are presented in Fig. 4 and B.1.

DCO^+ is detected in the 5–4 (PILS) and 3–2 (SMA) transitions, with a half-crescent shape centered around source A (Fig. 2 and 3). The peak is red-shifted and located ∼2″ southwest of source A in both transitions, consistent with the red-shifted emission of the disk-like structure to the southwest (Oya et al. 2016). Weak absorption is detected towards source B in the PILS observations, which is consistent with previous studies that indicate infall motions through an inverse P-cygni profile (Zapata et al. 2013). The DCO^+ emission south of source A is weak, peaking at 3 σ in the 5–4 transition and at 5σ in the 3–2 transition. It is slightly extended to the south along the outflow, but not as far as c$-C_3H_2$. In agreement with previous observations of DCO^+ and c$-C_3H_2$ for other objects (Spezzano et al. 2016a,b), these two molecules are spatially anti-correlated.

Five narrow (FWHM ≈ 1 km s^{-1}) lines of c$-C_3H_2$ in the 349 to 352 GHz frequency range with E_{up} ranging from 48 to 96 K are studied in this work. The emission peaks to the south

Table 2. Tests of the temperature and density profiles of the two sources.

	IRAS 16293-2422 (Crimier et al. 2010)			VLA 1623-2417 (Jørgensen et al. 2002)		
Test	T_{27AU} (K)	n_{27AU} (cm^{-3})	Note	T_{4AU} (K)	n_{4AU} (cm^{-3})	Note
1	300.0	2.36×10^{9}	unchanged	250.0	1.62×10^{9}	unchanged
2	300.0	2.36×10^{10}	n increased by 10	250.0	1.62×10^{10}	n increased by 10
3	300.0	2.36×10^{8}	n decreased by 10	250.0	1.62×10^{8}	n decreased by 10
4	100.0	2.36×10^{9}	T decreased by 3	166.7	1.62×10^{9}	T decreased by 1.5

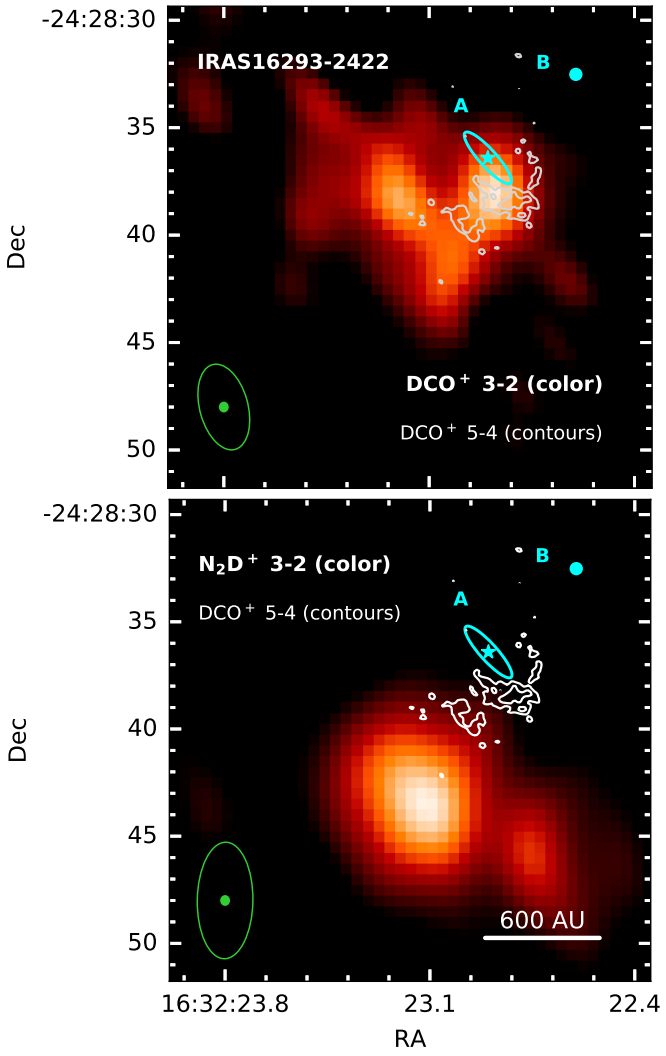

Fig. 3. Intensity integrated maps of DCO^+ 3–2 (top) and N_2D^+ 3–2 (bottom) observed with the SMA, overlaid with DCO^+ 5–4 (contours) observed with ALMA (combined 12m array and ACA). Contours are the same as in Fig. 2 with σ = 0.06 Jy beam^{-1}. The positions of IRAS 16293-2422 A and B are indicated with a star and circle, respectively. the cyan ellipse shows the disk-like structure. The filled green ellipses show the beam for the ALMA observations, while the unfilled ellipse shows the beam for the SMA observations. Both DCO^+ transitions match spatially, and N_2D^+ is located beyond the extent of the DCO^+ emission. Note the different center of this figure compared to Fig. 2.

of A, seen clearly in the top row of Fig. 2. The lines are also seen near source B, at one ALMA beam offset from the source. The southern emission extends from the circumstellar region of source A, and peaks at $\lesssim 5\sigma$ about ~4″ away from the source

Table 3. DCO^+ best approximation model parameters.

Parameter	IRAS 16293-2422	VLA 1623-2417
T_{peak} (K)	17–19	11–16
Drop boundaries:		
T_{sub} (K)	35	35
n_{de} (cm^{-3})	$\leq 10^6$	3×10^6
CO abundance:		
Inner X_{in}	10^{-5}	10^{-5}
Drop X_D	10^{-6}	10^{-7}
Outer X_0	10^{-4}	10^{-4}

position. Toward source A itself, the spectrum is too confused to identify the separate molecular lines. Thus the region is masked out in the maps within 2″ from the source position. Comparing c−C_3H_2 with H_2CO (Fig. 2) suggests that it could arise from one side of the southern outflow cavity wall. The asymmetric heating of the outflow cavity could be due to the behavior of the outflow from IRAS 16293 A. Observations of the outflow of IRAS 16293 A at large and small scales suggest that the outflow has shifted direction from east-west (dashed arrow shown in Fig. 1) to southeast-northwest (solid arrow shown in Fig. 1). The shift of outflow direction could have swept up material, thus causing the asymmetric morphology of the outflow cavity, and consequently c−C_3H_2 to only be present on one side of the outflow cavity. The emission around source B may either be from the circumstellar region or the outflow cavity, but due to the orientation it is difficult to say.

C_2H is clearly detected in both spin doubling transitions with each transition showing a characteristic double hyperfine structure pattern. The emission within 2″ of source A is masked out due to contamination from other molecular species. C_2H emission is located in a filament-like structure extending from north to south, passing through source B (Fig. 2). A second, weaker structure formed by a string of clumps extends from north-east to south-west, apparently passing through source A. C_2H is diffuse and weak, peaking at $\lesssim 5\sigma$ on all off-source positions on the map (Fig. 4). The emission around source B is brighter, peaking at 10σ in the intensity integrated map. From the channel map, the emission appears to have a subtle velocity gradient from north to south at source B. However, the C_2H emission does not match the structure and extent of c−C_3H_2 (or H_2CO) in either transition (Fig. 4 and B.1). It should be noted that neither C_2H or c−C_3H_2 coincide with the dust ridge seen in the continuum emission (Fig. 2; see also Jacobsen et al. 2018).

N_2D^+ 3–2 is mostly resolved out in the PILS survey, but it is detected south-east of DCO^+ with the SMA (Fig. 3), located 7″ away from the continuum position of source A with a S/N = 7 (Jørgensen et al. 2011). Similar to DCO^+, there is no N_2D^+ emission towards B. No transition of N_2D^+ was covered in the Band 7 observations.

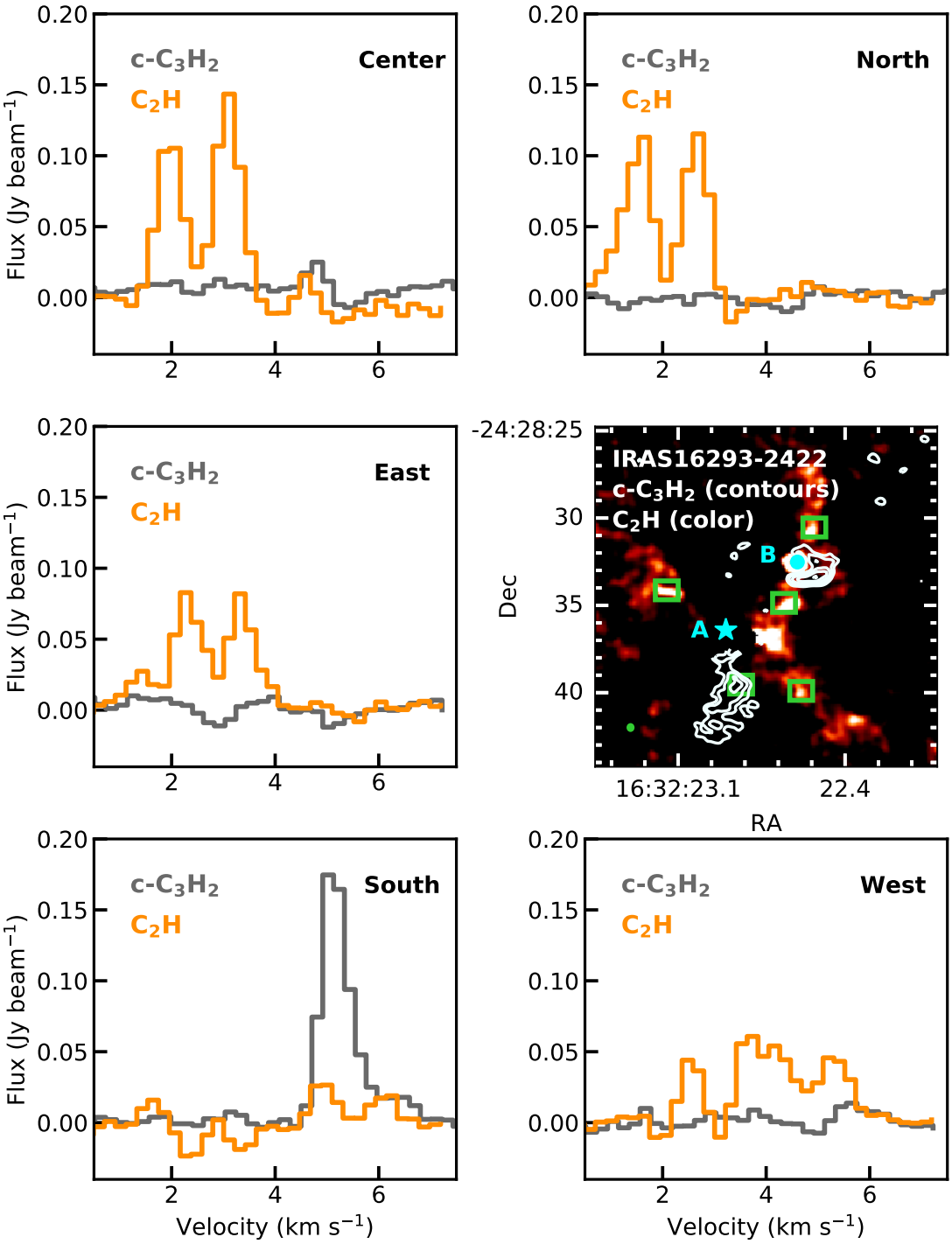

Fig. 4. IRAS 16293-2422 c−C_3H_2 5–4 and C_2H 4–3 J=9/2–7/2 spectra taken at 5 positions, indicated by the green boxes in the intensity integrated map presented in the center right panel, while the green circle on the bottom left indicates the beam of the combined 12m and ACA observations. The anti-correlation of both molecules is seen at all positions. The region within a radius of 2″ from the position of source A is contaminated by other molecular species, and is masked out for these maps.

3.2. VLA 1623-2417

Two transitions of DCO^+ and one transition each of c−C_3H_2, N_2H^+ and N_2D^+ were observed with ALMA in Bands 6 and 7. Additional APEX observations detected two transitions of DCO^+ and C_2H. Intensities and line widths are listed in Table 1. Fig. 5 shows the intensity integrated maps for the ALMA observations. All of these molecules trace material associated with VLA 1623 A, but not the other two components of the system, VLA 1623 B and W.

The DCO^+ 3–2 ALMA 12m array and ACA observations have been separately analysed in detail in Murillo et al. (2015). The 3–2 ACA map shows a smooth distribution peaking south-west of the source, with the blue-shifted emission extending north-east, but no clear red-shifted counterpart south-west. Here we present additional ALMA Band 7 12m array observations of DCO^+ 5–4. In both transitions of DCO^+ the red-shifted emis-

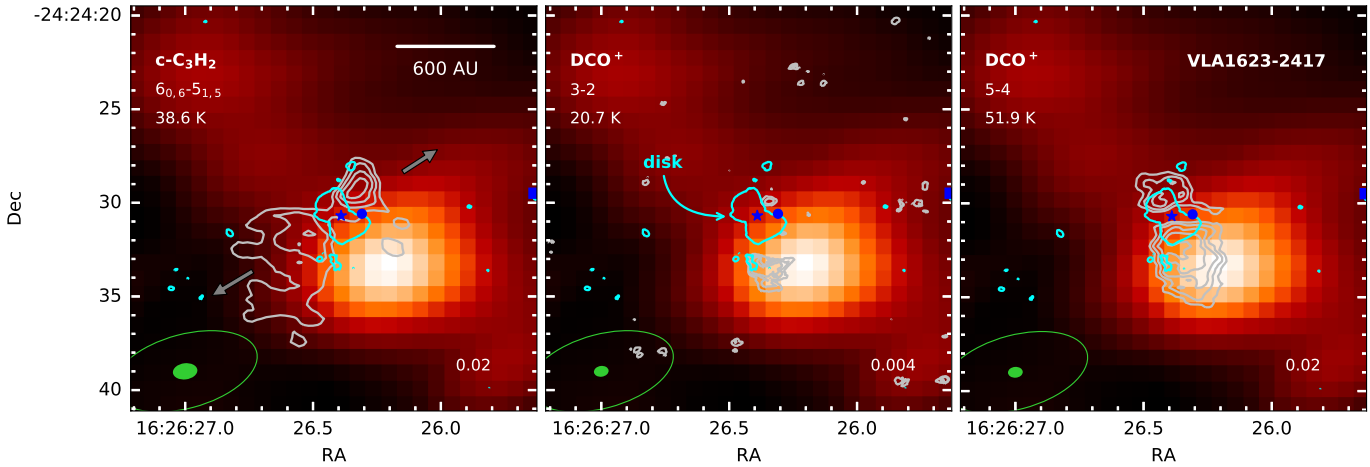

Fig. 5. Intensity integrated maps of (white contours) of c–C_3H_2 and DCO^+ (12m array) towards VLA 1623-2417. DCO^+ 3–2 from ACA observations is shown in color-scale. The gray arrows on the left panel show the outflow direction. The cyan line is the 3σ contour of $C^{18}O$ in order to show the location and extent of the rotating disk centered on VLA 1623-2417 A. Gray contours show the respective lines in steps of 3, 4, 5 and 6σ, except for DCO^+ 3–2 where the contours start at 4σ. The value of σ (Jy beam^{-1} km s^{-1}) is indicated in the lower right of each panel. The positions of VLA 1623-2417 A, B and W are indicated with a star, circle and square, respectively. The filled green ellipses show the beam for the 12m array observations (contours), while the unfilled ellipse shows the beam of the ACA observation (color-scale).

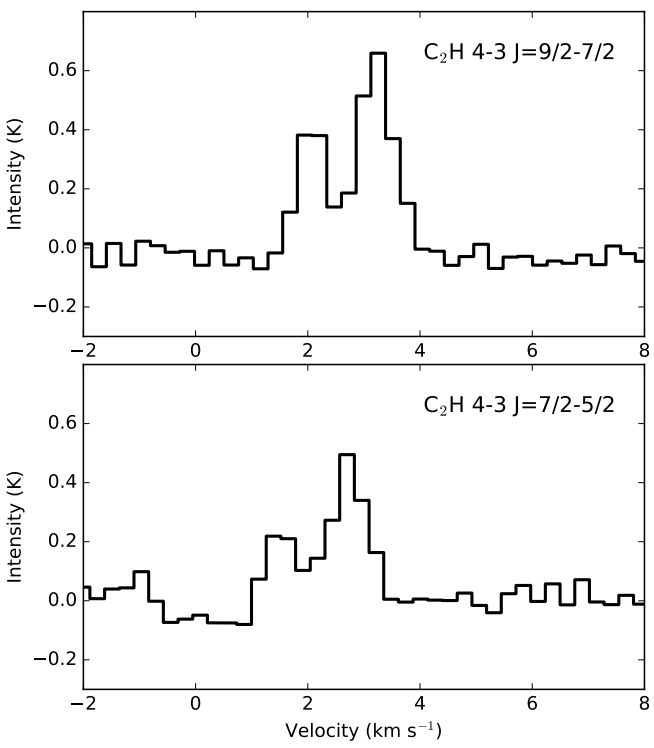

Fig. 6. Single pointing APEX observations of C_2H centered on VLA 1623 A.

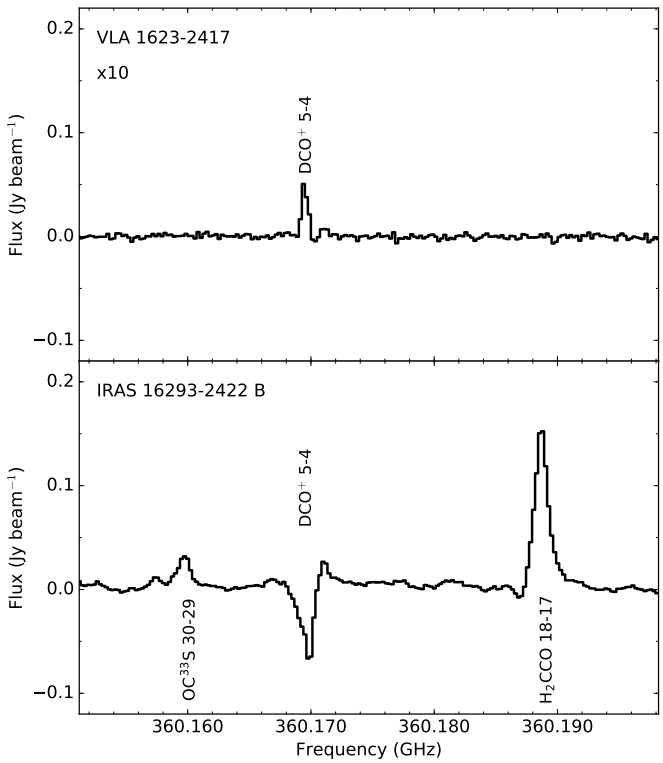

Fig. 7. Comparison of the spectra centered on DCO^+ 5–4 of VLA 1623-2417 A (12m array) and one beam offset from IRAS 16293-2422 B (combined 12m array and ACA). The spectra for VLA 1623-2417 has been multiplied by a factor of 10 in order to compare more easily. Note the lack of molecular line emission toward VLA 1623-2417 in contrast to IRAS 16293-2422.

sion, located to the south of VLA 1623 A, is clearly seen and is stronger than the blue-shifted emission located to the north. The DCO^+ 5–4 emission is three times stronger than the 3–2 emission with the 12m array, which makes the blue-shifted emission clearly visible. For both transitions the velocity gradients are consistent. The DCO^+ 3–2 emission borders the disk structure observed to be driven by VLA 1623 A and is relatively compact. Even more interesting, however, is that DCO^+ in the 5–4 transition extends closer to the position of VLA 1623 A than in the 3–2 transition (Fig. 5).

DCO^+ forms at temperatures below 20 K, where CO freezes out. The position of the DCO^+ 3–2 peak along the disk plane was

found to be the product of disk-shadowing, which causes a temperature drop at the edge of the disk, whereas along the outflow direction no such effect was observed (Murillo et al. 2015). The APEX observations of DCO^+ in both transitions show a single peak at the systemic velocity (3.7 – 4 km s^{-1}) and a peak intensity of 3.6 K for the 3–2 transition, the same as obtained from JCMT observations by Jørgensen et al. (2004). The beamsize for the APEX-1 and 2 Bands covers approximately the full extent of the DCO^+ emission seen in the ACA map. For the DCO^+ 3–2 transition, the ALMA observations recover about 28% of the flux detected in the APEX observations (117.1 Jy km s^{-1} with 24 Jy/K), while 20% was recovered with the DCO^+ 5–4 ALMA observations (APEX: 53.7 Jy km s^{-1} with 24 Jy/K).

One low-lying transition of c$-C_3H_2$ is detected with the short baselines of the 12m array, but not the long baselines. The detection of c$-C_3H_2$ with only the the short baselines of the 12m array indicates that the emission is extended without a compact structure component. The c$-C_3H_2$ emission is oriented perpendicular to the disk and seems to trace the cavity of the outflow driven by VLA 1623 A out to 3″ from the source position. There is no detection of c$-C_3H_2$ emission in the disk traced by $C^{18}O$ or at the disk-envelope interface, down to the noise level. The material along the outflow cavity exhibits signatures of rotation, most notable in the south-east lobe, with a velocity range and gradient direction similar to that of DCO^+ and $C^{18}O$ (Murillo et al. 2013). However, treating the kinematics of the outflow cavity wall traced by c$-C_3H_2$ is outside the scope of this paper, and will be presented in a separate paper.

C_2H is detected with APEX, with the hyperfine components of each transition being clearly distinguished (Fig. 6). Both transitions are located at the systemic velocity of VLA 1623 A (3.7 – 4.0 km s^{-1}) and show no broadening, indicating that the emission is most likely related to the envelope material of VLA 1623 A.

N_2H^+ and N_2D^+ are not detected in our ALMA observations. Possible reasons could be either due to the emission being very extended and thus resolved out in the interferometric observations, or the abundance of these molecules being too low to be detected. This is a surprising contrast to several other young embedded Class 0 sources which do show N_2H^+ and N_2D^+ (Jørgensen et al. 2004; Tobin et al. 2013). The non-detections of N_2H^+ and N_2D^+ are further analysed in Sect. 4.4. H_2D^+ is also not detected in our Cycle 2 Band 7 observations, this is consistent with the JCMT observations reported by Friesen et al. (2014). H_2D^+ is not further treated in this work.

4. Analysis

DCO^+ appears to peak offset from the protostellar positions bordering the disk-like structures in both sources (Fig. 2 and 5). Here we analyze the peak position first through chemical modelling of the observed emission (Section 4.1.1), and then using the line ratios to constrain the physical structure (temperature, density) and the associated chemistry (Section 4.1.2).

To study the physical conditions of the region traced by c$-C_3H_2$, line ratios of the detected transitions are used (Section 4.2). This is combined with C_2H to obtain the c$-C_3H_2$ / C_2H abundance ratio and show how the ratio varies with position (Section 4.3). c$-C_3H_2$ and C_2H can be produced by the destruction of large hydrocarbons through UV irradiation (top-down chemistry), or through the accumulation of C and H atoms to form small hydrocarbons (bottom-up). Because of the many different formation and destruction pathways, chemical modelling of these two molecules is not included in this work.

4.1. DCO^+

4.1.1. DCO^+ distribution

In Murillo et al. (2015) the distribution of DCO^+ around VLA 1623 was found to be altered by the presence of a rotationally supported disk, causing the emission to shift inwards along the disk plane but not along other directions. In this section, the DCO^+ emission around IRAS 16293 is modelled, aiming to find whether the distribution of DCO^+ in IRAS 16293 is product of the same phenomenon as observed in VLA 1623.

The DCO^+ chemistry is particularly sensitive to temperature. To model the observed emission for IRAS 16293 and VLA 1623, a simple steady-state, analytic chemical network that accounts for the basic reactions leading to the production and destruction of DCO^+ is used.

Since CO and H_2D^+ are the precursors of DCO^+, the production of H_2D^+ will be the rate-determining reaction in the chemical network, since it will dictate the production of DCO^+. The H_2D^+ production and destruction reaction is given by

$$H_3^+ + HD \underset{\Delta E}{\rightleftharpoons} H_2D^+ + H_2 \quad (1)$$

where the activation energy $\Delta E \sim 220$ K in the back reaction is due to the difference in zero-point energy. A crucial factor for deuterium chemistry is the ortho-to-para ratio of H_2 (Flower et al. 2006; Pagani et al. 2009b). This is included in the back reaction of the chemical network (Eq. 1), since it is here where the distinction has the most significant effect (Murillo et al. 2015). The reactions and parameters for o$-H_2$ and p$-H_2$ were adapted from Walmsley et al. (2004). The ortho-to-para ratio is set to have a lower limit of 10^{-3} at low temperatures, as constrained from observations and models (Flower et al. 2006). The rate coefficient for two-body reaction is expressed as

$$k = \alpha \left(\frac{T}{300}\right)^{\beta} \exp\left(-\frac{\gamma}{T}\right) \text{ cm}^3 \text{ s}^{-1} \quad (2)$$

where T is the temperature of the gas. For cosmic ray ionization, important in the generation of H_3^+, the rate coefficient is given by

$$k = \zeta \text{ s}^{-1} \quad (3)$$

where $\zeta = 1.26 \times 10^{-17}$ is the cosmic-ray ionization rate of H_2. The reactions and rate coefficients used in this work are the same as those listed in Murillo et al. (2015).

Since CO is a parent molecule of DCO^+, its abundance will impact the production of DCO^+. The profile of the CO abundance is taken to be either constant or with a drop used to simulate freeze-out. The drop is set by the CO sublimation temperature $T_{\rm sub}$ and desorption density $n_{\rm de}$. These limits dictate the boundary where CO is in the gas phase ($T > T_{\rm sub}$) or freezes onto the dust grains ($T < T_{\rm sub}$); and when the freeze-out timescales for CO are too long ($n < n_{\rm de}$) compared to the lifetime of the core (Jørgensen et al. 2005c). The results of the chemical modelling are passed through RATRAN (Hogerheijde & van der Tak 2000), and then synthetic data cubes are generated in order to directly compare with the observations. Because the DCO^+ emission is weak, the radial profile of the observations is obtained by using a cut with a width that covers the red-shifted peak. The model radial profile, on the other hand, is obtained from a simple cut to the synthetic data cubes since the models are symmetric flat disks. The network and further details of the model and post-processing are given in Murillo et al. (2015).

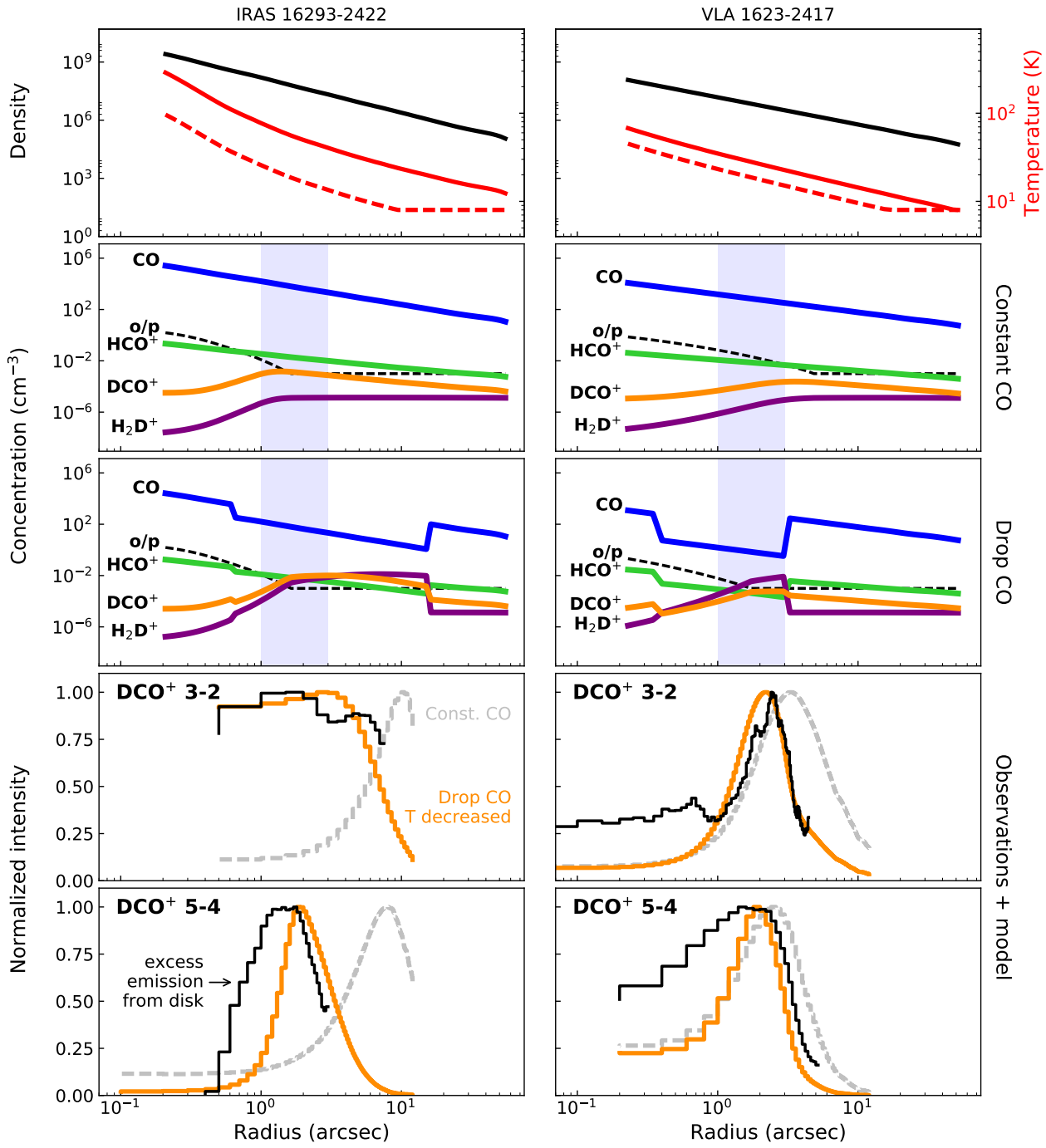

Fig. 8. Results from modelling the observed DCO^+ peak with our simple analytic chemical model. The left column shows results for IRAS 16293-2422, while the right column shows those for VLA 1623-2417. The top row shows the input density (black) and temperature (red) as functions of radius for each system. The solid red line shows the original temperature profile used for the constant CO model (second row panels). The dashed red line is the profile decreased by factors of 3 and 1.5 for IRAS 16293-2422 and VLA 1623-2417, respectively, and used for the drop CO model (third row panels). The lower limit on the temperature is set at 8K. In the second and third row, the shaded range is the location of the observed DCO^+ peak. The fourth and fifth rows show the observed radial profiles of DCO^+ (black lines) overlaid with both Constant (dashed gray lines) and Drop CO models (solid orange lines). In all panels, the protostellar source is located on the left, and the envelope on the right, with the peak position of DCO^+ indicating the disk-envelope interface. Note that the excess DCO^+ 5–4 emission from the disk(-like) regions is not well reproduced by the cold DCO^+ network.

The model requires a density and temperature profile of the source as a function of radius. For IRAS 16293, the power-law density and temperature profile from Crimier et al. (2010) is adopted. Two assumptions are made, namely that the density and temperature profile is centred on IRAS 16293 A and that it is the main contributor to the luminosity of the core, consistent with the recent analysis of Jacobsen et al. (2018). Crimier et al. (2010) also showed that the emission is dominated by one of the two components, most likely IRAS 16293 A, rather than being centered between the two sources. Thus, our assumptions

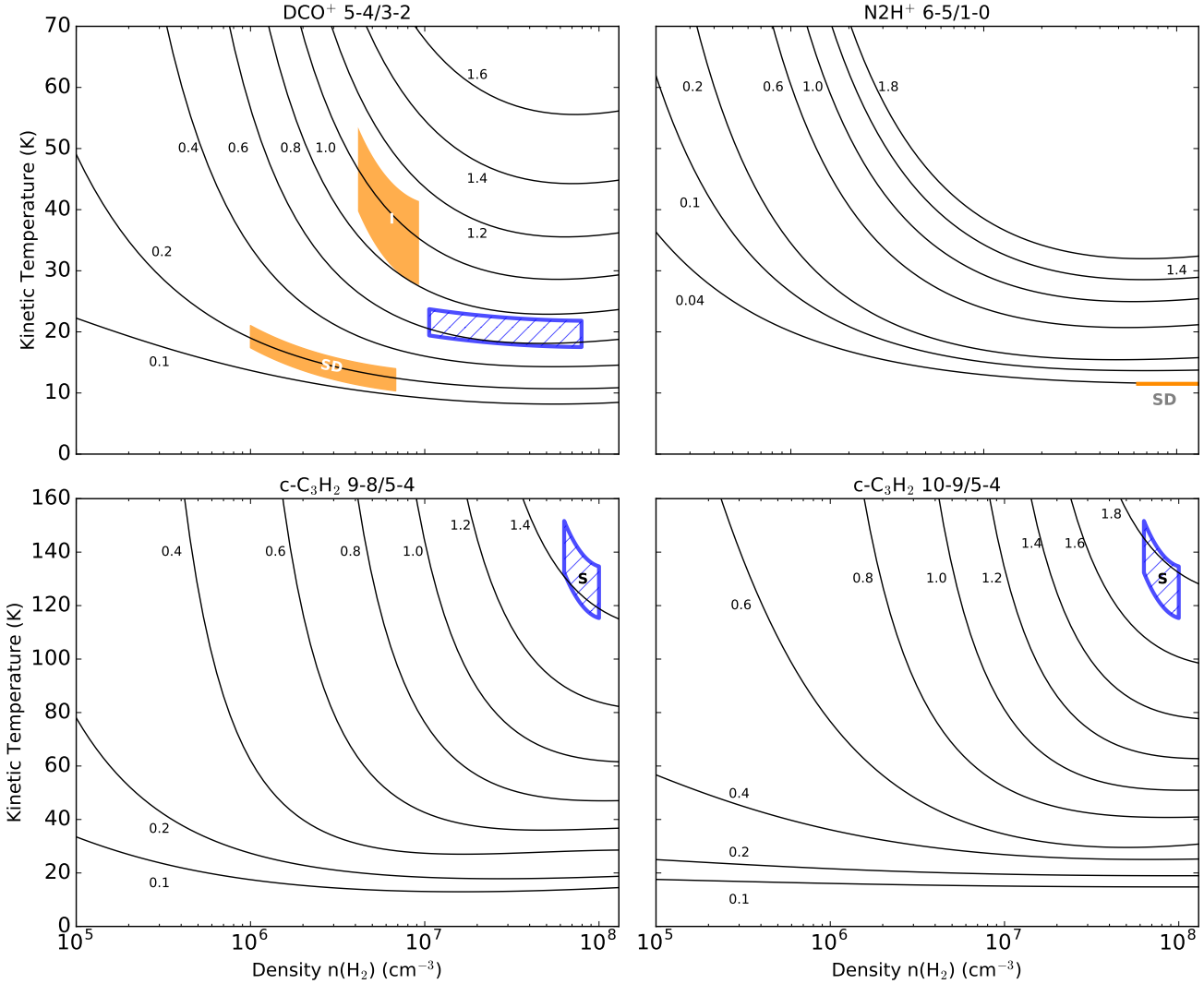

Fig. 9. Calculated line brightness temperature ratios for DCO^+ 5–4/3–2, N_2H^+ 6–5/1–0 and c−C_3H_2 10–9/5–4 and 9–8/5–4. Black lines show the modelled ratios assuming column densities of 2.5×10^{12} and 1.3×10^{13} cm^{-2} for DCO^+ and N_2H^+, respectively, and 7×10^{13} for both c−C_3H_2 ratios. Colored regions indicate the observed line ratios drawn over the range of densities and temperatures that characterize the observed emission, for IRAS 16293-2422 with ALMA (hatched blue) and VLA 1623-2417 (solid orange) with single-dish (SD) and interferometric (I) observations. For c−C_3H_2, the value for IRAS 16293 is from the south position.

should not introduce major issues in our modelling. While there have been several physical profiles derived for IRAS 16293 (e.g., Schöier et al. 2002), only one is adopted here since we alter the density and temperature profiles by an arbitrary factor, exploring the effects of these parameters on the production of DCO^+. For VLA 1623, we adopt the power-law density and temperature profile from Jørgensen et al. (2002). Here again we assume the density and temperature profile is centred and dominated by VLA 1623 A. Given that VLA 1623 B does not contribute much to the line emission nor the continuum, and that VLA 1623 W is 10″ away, this should not produce issues in the resulting model. The temperature and density profile for VLA 1623 is also altered by an arbitrary factor to study the effect on DCO^+ production. The variations in the temperature and density profiles used in this work are listed in Table 2 for both systems.

For the DCO^+ models, we explore the parameter ranges of T_{sub} = 20–40 K, n_{de} = 10^5–10^8 cm^{-3} and X[CO] = 10^{-7} – 10^{-4}. The parameters for the best by-eye approximation to the observed DCO^+ peak position are listed in Table 3 for both systems. The best approximated model of the DCO^+ 3–2 emission around VLA (Murillo et al. 2015) are reproduced here and compared with the results of DCO^+ toward IRAS 16293.

For both systems we find that the constant CO abundance profile produces a DCO^+ peak further out than where it is observed (gray dashed line in fourth and fifth rows of Fig. 8), and the peak position does not shift with a change in the abundance (Murillo et al. 2015). The drop CO abundance profile produces a peak within the drop boundaries, T_{sub} and n_{de}. Altering these parameters changes the shape but not the position of the DCO^+ peak (See Murillo et al. 2015).

Since the chemical conditions do not alter the peak position, the physical structure is examined. The original source density and temperature profiles for both sources also do not reproduce the position of the DCO^+ peak. Increasing or decreasing the density by one order of magnitude, causes the DCO^+ peak to either shift outwards or remain at a position similar to the unchanged density profile. Interestingly, only reducing the temperature profile by an arbitrary factor together with the drop CO abundance profile, causes the DCO^+ peak to shift inwards for both systems (orange solid line in Fig. 8). A by eye fit of the chemical model to

Table 4. DCO^+ intensities and line ratios, with inferred temperature and density.

Source	IRAS 16293-2422		VLA 1623-2417 - ALMA		VLA 1623-2417 - APEX	
Transition	5–4 (ACA)	3–2 (SMA)	5–4	3–2	5–4	3–2
Line width (km s^{-1})	1.0	1.0	0.6	0.6	0.7	0.7
Beam (arcsec)	5.25×2.36	4.11×2.45	0.87×0.65	0.85×0.54	17.3	28.9
Peak (Jy $beam^{-1}$)	3.8±0.6	1.9±0.2	0.29±0.02	0.087±0.008	...	...
Peak (K)	2.9±0.4	4.9±0.6	4.8±0.3	4.9±0.5	0.79±0.1[a]	4.8±0.1
Line ratio	0.6±0.1		1.0±0.1		0.2±0.03	
Column density (cm^{-2})	3×10^{12}		2×10^{12}		2×10^{12}	
H_2 density (cm^{-3})	$1–8\times10^7$		$2–6\times10^6$		$1–6\times10^6$	
Kinetic Temperature (K)	20–23		30–55		12–19	
τ	<1		<1		<1	

Notes. [(a)] Peak temperature with beam dilution factor applied to DCO^+ 5–4 (see Appendix C), taking the beam to be 17.3″, and source 28.9″.

Table 5. $c–C_3H_2$ inferred parameters and abundance ratio for $c–C_3H_2/C_2H$

Position	Coordinates		9–8/5–4	10–9/5–4	n_{H_2}	T_{kin}	$N_{c–C_3H_2}$ [a, b]	N_{C_2H} [a]	$c–C_3H_2/C_2H$
	RA	Dec			cm^{-3}	K	cm^{-2}	cm^{-2}	
IRAS 16293-2422									
South	16:32:22.88	–24:28:39.78	1.4±0.07	1.7±0.08	$5–10\times10^7$	120 – 155	9.3×10^{13}	$\leq3\times10^{13}$	≥3.1
Center	16:32:22.69	–24:28:35.16			$1–6\times10^{7c}$	50 – 120	$5 – 7\times10^{12}$	2×10^{14}	≤0.035
North	16:32:22.55	–24:28:30.28			$1–6\times10^{7c}$	50 – 120	$5 – 7\times10^{12}$	2×10^{14}	≤0.035
VLA 1623-2417 $c–C_3H_2$ $6_{0,6}–5_{1,5}$									
$c–C_3H_2$[e]	16:26:26.39	–24:24:30.69	...	...	$5–10\times10^7$	120–155	$5.3–6.7\times10^{10}$	3×10^{13}	0.002[e]

Notes. [(a)] For IRAS 16293-2422, column densities are for a beam of 0.5″. For VLA 1623-2417, column densities are for a beam of 17.3″, corresponding to the beam of the C_2H observations. [(b)] An o/p = 3 was used to calculate the total column density of $c–C_3H_2$. [(c)] Densities are assumed from the model envelope. [(d)] $c–C_3H_2$ n_{H_2} and T_{kin} parameters taken from the south position of IRAS 16293-2422. [(e)] Due to the different scales being picked up by the observations, the ratio is not well determined, and is provided here for reference.

the observations is used to constrain the decrease in the temperature profile (Fig. 8). The factor is constrained to be 1.5+/-0.2 for VLA 1623 and 3.0+/-0.2 for IRAS 16293. This is consistent with the results found for VLA's DCO^+ 3–2 in Murillo et al. (2015), which explores the physical and chemical parameter space in more detail. Thus the observed DCO^+ peak position is produced by a drop in the temperature along the plane perpendicular to the outflow(s). This drop in temperature can be caused by a structure, such as a disk, which shadows the outer regions, allowing the peak emission of molecules whose abundance is enhanced in cold gas to move inwards.

It should be noted, however, that our simple chemical model cannot fully explain the inner part of the DCO^+ 5–4 emission observed toward VLA 1623 A and IRAS 16293 A (orange and black solid lines in the bottom row of Fig. 8). DCO^+ 5–4 emission at small radii could be located in the disk where both cold and warm chemical processes can contribute to its formation (Favre et al. 2015; Huang et al. 2017; Salinas et al. 2017). For warm DCO^+ to form, gas with temperatures up to 70 K (Favre et al. 2015) are needed. DCO^+ 5–4 is observed further into the disk of VLA 1623 A (L_{bol} = 1 $L_\odot$, Murillo & Lai 2013) than in IRAS 16293 (L_{bol} = 18 $L_\odot$, Jacobsen et al. 2018) due to the lower temperature of the inner disk regions. Considering the original source profile which applies to the disk region (top row, solid red line, Fig. 8), IRAS 16293 A reaches gas temperatures of 70 K at about 1″ or 120 AU, the outer part of the 200 AU disk-like structure (Oya et al. 2016). In contrast, VLA 1623 A reaches 70 K at 0.1″ or 12 AU – i.e., significantly closer to the protostar.

Thus, the distribution of the cold DCO^+ around both VLA 1623 and IRAS 16293 is product of the presence of a disk(-like) structure, which causes a drop in temperature on the envelope gas at the edge of the disk(-like structure), i.e. the disk-envelope interface. The presence of the disk(-like) structure generates an asymmetric temperature profile in the protostellar system.

4.1.2. Line ratios and implied physical conditions

Line ratios can provide an independent measure of the temperature of the region being traced by a molecule. The ratio of DCO^+ 5–4/3–2 will provide an independent test of the results obtained with the chemical model of DCO^+ described in the previous section.

Using RADEX (van der Tak et al. 2007), we performed non-LTE excitation and radiative transfer calculations to constrain the temperature and density of the regions being traced by comparing the ratios of observed molecular lines with those calculated by the non-LTE excitation. We limit the range of H_2 densities based on the source profile used for chemical modelling (Table 2 and Fig. 8) and the radial position of the emission being modelled. Using RADEX the column density of the emission was checked to see if it is produced by molecular line emission that is optically thin or thick at H_2 densities of $1–8\times10^7$ cm^{-3} for IRAS 16293 and $2–6\times10^6$ cm^{-3} for VLA 1623. For the best-fitting column densities of $(2-3)\times10^{12}$ cm^{-2} and densities of $10^6–10^8$ cm^{-3}, the DCO^+ 3–2 and 5–4 emission is optically thin in both sources (Table 4). To produce optically thick lines, column densities of $>7\times10^{12}$ cm^{-2} would be needed for a temperature of 20 K. As the emission of both lines are optically thin, the line intensity ratios are not affected by the adopted column density. All the molecular data files used in this work are obtained from the Leiden Atomic and Molecular Database (LAMDA; Schöier

et al. 2005). The collisional rate coefficients for DCO^+ are based on the results of (Botschwina et al. 1993) and (Flower 1999). In order to compare the observed peak intensities with the results from RADEX, the observed peak intensities are converted from Jy beam^{-1} to K using the relation $T_{\rm mb} = 1.36\ \lambda^2/\theta^2\ I_{\nu,\rm obs}$ where λ is the wavelength in centimetres of the molecular transition, θ is the beam of the observations and $I_{\nu,\rm obs}$ is the observed peak intensity in mJy beam^{-1}.

Here, we derive the physical parameters from the DCO^+ 5–4/3–2 ratio for both sources. Figure 9 shows the variation of the DCO^+ 5–4/3–2 ratio with H_2 density and temperature. For both IRAS 16293 and VLA 1623, the red-shifted peak emission is considered, since it is the most prominent. The results for IRAS and VLA 1623 are compared in Table 4.

For IRAS 16293, a ratio DCO^+ 5–4/3–2 = 0.6 ± 0.1 is obtained from the PILS Band 7 observations and the SMA 230 GHz observations (Jørgensen et al. 2011). Note that for IRAS 16293, we only use the peak intensity from the ACA observations, and thus pick up emission from scales similar to the SMA observations. Thus beam dilution does not need to be taken into consideration. We adopt a line width of 1.0 km s^{-1} and a column density of 3×10^{12} cm^{-2}, a value that also reproduces the observed line intensities. For densities below 10^6 cm^{-3}, the critical density of the 5–4 transition, the line ratio is primarily sensitive to density; at higher densities, the ratio becomes a good temperature probe. According to the density structure presented in Fig. 8 (top panel), the density at the peak DCO^+ emission position is higher than the critical density, so a kinetic temperature between 20 and 23 K can be inferred for IRAS 16293. This temperature is consistent with the chemical modelling of the DCO^+ peak position.

For VLA 1623, the ALMA 12m array observations provide DCO^+ 5–4/3–2 = 1.0 ± 0.1. The beam-size of DCO^+ 5–4 (0.87″×0.65″) is similar to that of the 3–2 transition (0.87″×0.54″) and thus no beam dilution factor was added to the calculation. This line brightness temperature ratio implies a kinetic temperature between 30 and 55 K, adopting a column density of 2×10^{12} and a line width of 0.7 km s^{-1} to reproduce the observed peak intensities. This is higher than expected from the chemical modelling of DCO^+. The APEX observations are used to double check if this is the kinetic temperature of the bulk of the DCO^+ emission at the disk-envelope interface. The APEX DCO^+ data give a much lower line ratio, 5–4/3–2 = 0.2 ± 0.03. This line brightness temperature ratio is well reproduced by a kinetic temperature of 12 to 19 K, in agreement with the chemical model. It is likely that the ALMA 12m array observations are picking up both warm and cold DCO^+ emission in the 5–4 transition, but only cold DCO^+ in the 3–2 transition. On the other hand, the APEX observations are recovering DCO^+ emission from the cold regions at the edge of the disk and the envelope, but the beam size dilutes the emission from the inner regions. This then causes the discrepancy of derived kinetic temperatures that we obtain from interferometric versus single-dish data. The temperature from the interferometric data is driven up due to more emission being detected in the higher transition.

4.2. c−C_3H_2 excitation

Five transitions of c−C_3H_2 are detected towards IRAS 16293. Temperature is derived from the c−C_3H_2 9–8/5–4 and 10–9/5–4 ratios following the same method as in Section 4.1. The collisional rate coefficients for c−C_3H_2 are based on Chandra & Kegel (2000). The density range is chosen based on the envelope model of IRAS 16293. Figure 9 shows the the line brightness temperature ratios as functions of H_2 density and kinetic temperature. The ortho-c−C_3H_2 molecular file is used for the RADEX calculations since the 5–4 transition (349.264 GHz) presented here is the ortho form (para-c−C_3H_2 5–4 is at 338.204 GHz). To convert to the total (ortho + para) c−C_3H_2 column density, an o/p ratio of 3 was used. Three regions covering the south c−C_3H_2 peak and the C_2H peaks near the center and north of the map are selected to derive the temperature and c−C_3H_2/C_2H column density ratios (Fig. 4). For the position with no detections of either molecule, the peak intensity from within the box used to probe the respective position (Fig. 4) is used. These values are listed in Table C.1. Table 5 lists the positions. The IRAS 16293 A and B positions are not modelled due to contamination from other molecular species.

Both c−C_3H_2 9–8/5–4 and 10–9/5–4 ratios are simultaneously fit for the south position. For the center and north positions, a temperature of 50 to 120 K is assumed and the column density is calculated assuming an upper limit of 3 times the rms noise for the peak temperature brightness. Table 5 lists the derived kinetic temperature from the c−C_3H_2 ratio together with the assumed c−C_3H_2 column densities for the regions being traced. The total column density for c−C_3H_2 is calculated assuming an ortho-to-para ratio of 3. The peak intensities for each transition are listed in Table C.1 We find that the temperature for the south c−C_3H_2 peak, corresponding to the outflow cavity of IRAS 16293 A , is between 120–155 K. Comparing the temperatures obtained from c−C_3H_2 and DCO^+ line ratios, it is clear that c−C_3H_2 arises from a much warmer region than DCO^+. This is linked to the spatial anti-correlation found for these two molecules, both in our observations and other work (see Sect. 5).

Only one transition of c−C_3H_2 is available for VLA 1623, with an upper level energy (38.6 K) lower than those observed toward IRAS 16293 (≥ 49 K). Thus to obtain an idea of the column densities in the region traced by c−C_3H_2 towards VLA 1623, we adopt the temperature and density from the c−C_3H_2 line ratios towards IRAS at the south peak. The c−C_3H_2 south peak of IRAS 16293 is chosen due to the fact that it traces the outflow cavity, as it does for VLA 1623. Using the parameters of c−C_3H_2 from the south position of IRAS 16293, the derived column density is $2{\times}10^{13}$ cm^{-2} for a beam of 1.6″×0.88″, lower by about a factor of 5 than that found for the south peak of IRAS 16293 and similar to the column density found for the central position of the IRAS 16293 map. If the beam from the C_2H observations is considered (17.3″), the derived column density of c−C_3H_2 becomes a few 10^{10} cm^{-2} (Table 5).

4.3. c−C_3H_2 / C_2H abundance ratio

The same transitions of C_2H are observed towards both sources, with ALMA for IRAS 16293 and with APEX for VLA 1623. The peak intensities are listed in Table C.1. Since C_2H ratios are not sensitive to temperature or density given the similar upper eneriges $E_{\rm up}$ (Table 1), the method adopted for DCO^+ and c−C_3H_2 cannot be used here. Instead, the C_2H column density is derived by assuming the kinetic temperature and number density obtained from c−C_3H_2 line ratios. Using the same derived temperature and density for C_2H from c−C_3H_2 for the corresponding position is done to probe the parameters of C_2H if it is tracing the same region as c−C_3H_2. The results are listed in Table 5.

The south position in IRAS 16293 presents a column density of $\leq 3{\times}10^{13}$ cm^{-2} for C_2H, about an order of magnitude lower compared to the centre and north positions which have a column density of $2{\times}10^{14}$ cm^{-2}. Table 5 lists the c−C_3H_2/C_2H column

density ratio for each position. It must be noted that the ratio at the south position is a lower limit, whereas for the central and north position, it is an upper limit. The differences in ratios between positions reflect the anti-correlation of the two molecules in the IRAS 16293 system. Most certainly, the anti-correlation is not due to critical densities, since the derived number densities of c−C_3H_2 (10^7 to 10^8 cm^{-3}) at all points are above the critical densities of both C_2H (8×10^4 to 6×10^5 cm^{-3}) and c−C_3H_2 ($2–5\times10^5$ cm^{-3}).

For VLA 1623, C_2H column densities are found to be a few times 10^{13} cm^{-2}, lower than the peaks of C_2H detected towards IRAS 16293. The difference in column densities are most likely be due to beam dilution effect from the observations with APEX. Thus the c−C_3H_2/C_2H ratio is not well determined for VLA1623. The results are listed in Table 5.

4.4. N_2H^+ and N_2D^+

For VLA 1623, the ALMA 12m array observations of N_2D^+ and N_2H^+ did not detect any emission. Since these molecules are readily detected in other sources (e.g., Tobin et al. 2013), the cause of this non-detection is examined. Two cases are explored, extended and compact emission concentrated in a 1″ region. The details of the analysis are given in Appendix C.

For the case of extended emission, the predicted N_2H^+ 4–3 peak intensity is the same as the noise level of our observations, while for the case of the emission concentrated in 1″ region, the S/N would be about 26. In a similar manner, the predicted N_2D^+ 3–2 peak intensity is expected to have a marginal detection in our observations for the extended emission case, and a $S/N = 40$ for the compact emission case. Thus, we should have detected both molecules in our observations if they arose from a compact structure.

5. Discussion

5.1. Comparison of IRAS 16293-2422 and VLA 1623-2417

The chemical structure of both systems is compared in this section. A cartoon of their structure is shown in Fig. 10.

The DCO^+ peak position in both sources is well described by a drop in the temperature profile. This drop can be explained by the presence of a disk which shadows the envelope, causing the DCO^+ emission to move inward, closer to the source along the disk plane. For VLA 1623, the ALMA DCO^+ 5–4 observations are picking up emission coming from both the cold envelope at the edge of the disk (disk-envelope interface) and the warmer parts of the disk.

c−C_3H_2 traces the outflow cavity wall of IRAS 16293 A and VLA 1623 A. Due to c−C_3H_2 having both top-down and bottom up chemistry, it was not studied using a chemical model. For VLA 1623 A, c−C_3H_2 traces the full outflow cavity (extending out to 3″), whereas for IRAS 16293 A only one side of the south outflow cavity wall is observed. It is possible that the c−C_3H_2 emission is product of UV radiation from the central source, and the warmer temperatures found in the outflow cavity. UV radiation liberates atomic carbon which leads to gas-phase formation of small hydrocarbons. Chemical models of the outflow cavity walls show that c−C_3H_2 is initially concentrated around the outflow wall, and progressively moves to the disk plane as the cavity widens with age, irradiating more envelope material (Drozdovskaya et al. 2015). Higher temperatures could accelerate certain chemical processes in the protostellar envelope,

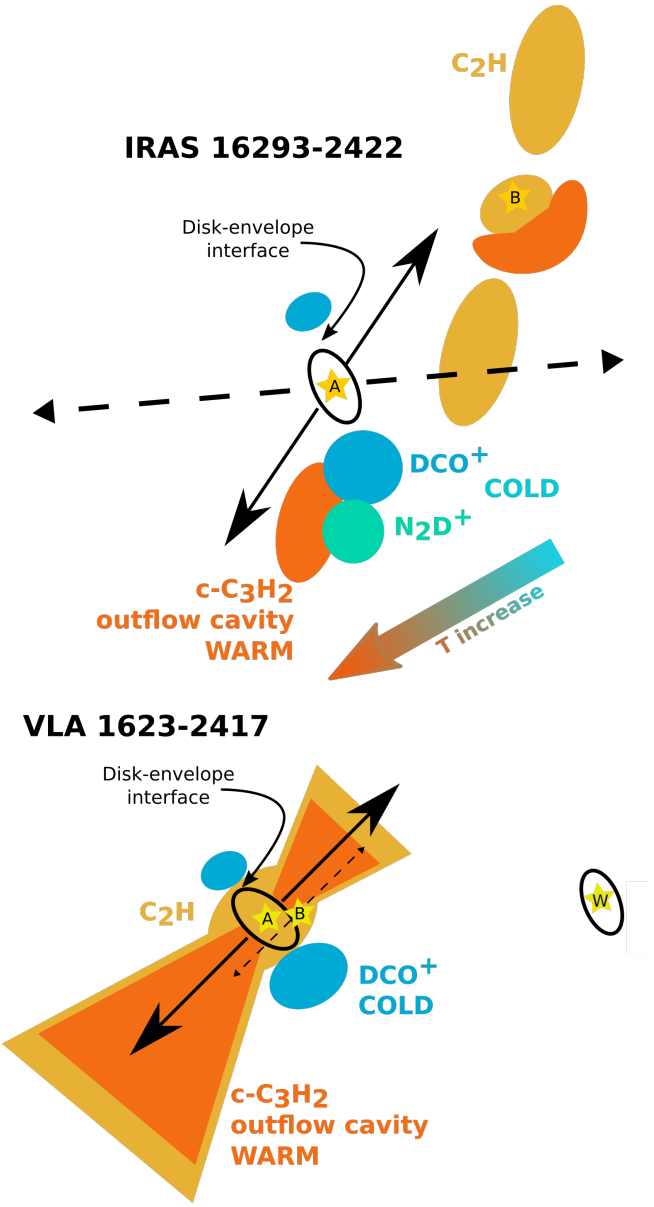

Fig. 10. Cartoon showing the distribution of the molecules studied in this work towards both sources. The solid and dashed lines show outflow directions. Black ellipses indicate disk structures. C_2H toward VLA 1623A is observed with APEX, thus the distribution is expected based on the physical conditions of VLA 1623, instead of direct mapping.

while movement of material through outflows, rotation and infall could bring dust with c−C_3H_2 precursors (e.g., CH_4, C_2H_2) closer to areas where they can be sublimated and thus enhance the c−C_3H_2 gas. Hence, the differences in the spatial distributions of c−C_3H_2 in IRAS 16293 A ($L_{bol} > 18$ L$_\odot$, Jacobsen et al. 2018) and VLA 1623 A (L_{bol} ~1$L_\odot$) could be the product of age, luminosity, or core dynamics. In any case, the presence of c−C_3H_2 emission is due to the temperature of the region where it is observed.

C_2H does not present similar distributions in IRAS 16293 and VLA 1623. For VLA 1623, the single-dish observations of C_2H showed no emission was detected in the off positions, thus we expect that C_2H peaks around VLA 1623 A. Given the observations, low temperatures in the envelope of VLA 1623 A as well as the envelopes of VLA 1623 B and W, and the forma-

tion mechanism of the two molecules, it might be possible that C_2H is spatially correlated with c$-C_3H_2$ on ∼15″ scales. However, interferometric observations are needed to verify if both molecules are correlated toward VLA 1623. On larger scales, part of the C_2H could also come from the envelope, given that it shows similar broadening with DCO^+ (Lindberg et al. 2017).

For IRAS 16293, the observed C_2H is found in the region one beam away from IRAS 16293 B, but does not show relation with the position or outflow of IRAS 16293 A, nor with the dust ridge connecting both sources. Beyond IRAS 16293 B, C_2H and c$-C_3H_2$ are not spatially correlated (Fig. 4 and B.1). This anti-correlation is unexpected from chemical models (e.g. Gerin et al. 2011; Drozdovskaya et al. 2015; Guzmán et al. 2015) or observations (see Sect. 5.2). The c$-C_3H_2/C_2H$ ratio is expected to be lowered with age, that is as the protostar evolves (O. Sipilä, private communication). If the different distributions of c$-C_3H_2$ and C_2H are product of age, it would suggest that IRAS 16293 and VLA 1623 are young; however, lowering the ratio with age does not explain the anti-correlation observed within IRAS 16293.

A possible explanation may be top-down chemistry producing small hydrocarbons through UV destruction of large aromatic molecules as inferred for lower density PDRs (Guzmán et al. 2015), producing different amounts of the two molecules. Another possibility for the anti-correlation might be explained by the destruction of C_2H in reactions with sulfur, nitrogen, oxygen or carbon chains (Sakai & Yamamoto 2013). The full Band 7 spectrum is examined at the c$-C_3H_2$ peak position (Fig. D.1–D.3) in order to examine whether products of C_2H reactions are present. C_2S, product of C_2H reacting with sulfur (Drozdovskaya et al. 2018), is not detected. In fact, little else is observed in the dense gas south of IRAS 16293 A. Apart from c$-C_3H_2$, only H_2CS (Drozdovskaya et al. 2018) and a few common species like HCO^+, H_2CO and CH_3OH are detected, which is unexpected given that outflow cavity would be irradiated and encourage chemical complexity (Drozdovskaya et al. 2015). Reactions of C_2H with carbon chains C_n would cause production of C_{n+2} and hydrogen, rendering these products undetectable due to lack of dipole moments. Overall, the strong anti-correlation of these molecules remains a chemical puzzle.

N_2D^+ is detected 7″ south of IRAS 16293 A with the SMA (Fig. 3), bordering the DCO^+ emission (Jørgensen et al. 2011). In contrast, N_2D^+ and N_2H^+ are not detected with ALMA observations towards VLA 1623. Single-dish observations show an offset of about 60″ between the position of VLA 1623 and the peak of N_2H^+ and N_2D^+ (Di Francesco et al. 2004; André et al. 2007; Liseau et al. 2015; Punanova et al. 2016; Favre et al. 2017). Line ratios of N_2H^+ and N_2D^+ from single-dish observations were investigated in Section 4.4 and Appendix C, where it was found that ALMA would detect only compact emission. Given the lack of ALMA detection of both molecules, N_2D^+ and N_2H^+ trace extended emission outside the envelope of VLA 1623 (Liseau et al. 2015).

The presence of N_2D^+ in IRAS 16293, but not in VLA 1623, could be product of temperature differences. N_2 can be frozen out onto dust grains at temperatures below 20 K (Bisschop et al. 2006), a scenario also pointed out by Di Francesco et al. (2004). While other nitrogen-bearing molecules such as CN, HCN, HNC and NO can form in the gas and on grain surfaces, N_2H^+ and N_2D^+ only form in the gas phase if N_2 gas is present. This scenario is further supported by the low temperatures found for DCO^+. For VLA 1623 A, DCO^+ has T_{kin} = 17 K, and the chemical modelling suggests dust temperatures between 11 to 16 K for where DCO^+ peaks. This would indicate that further out, the temperature is even lower. In addition, at densities below $\sim 10^4$ cm^{-3} (two orders of magnitude below what is derived from DCO^+ for VLA 1623), the dust and gas temperatures decouple, and without any additional external pressure, the gas temperature drops down to 10 K (Galli et al. 2002; Evans et al. 2001), which could cause N_2H^+ and N_2D^+ to recombine onto the dust grains or the precursor N_2 to freeze-out. In contrast, DCO^+ south of IRAS 16293 A indicates T_{kin} = 20 to 23 K for the gas, and dust temperatures between 17 to 19 K from chemical modelling, evidencing that the envelope of IRAS 16293 A is warmer than that of VLA 1623 (Jacobsen et al. 2018).

N_2H^+ and N_2D^+ are thought to be tracers of evolutionary stage (Emprechtinger et al. 2009), as well as of the CO snowline (Jørgensen et al. 2004; Anderl et al. 2016; van't Hoff et al. 2017). These assumptions break down for very cold envelopes of embedded protostars, like that of VLA 1623. Given that some starless cores do show N_2H^+ and N_2D^+ (e.g. Crapsi et al. 2005; Tobin et al. 2013), including the starless cores north of VLA 1623 (Di Francesco et al. 2004; Friesen et al. 2014), it cannot be said that the cold envelope itself is an indicator of evolutionary stage. It may be possible that the ridge of material north of VLA 1623, which contains the starless cores, is being heated somehow from the side, but VLA 1623 is being shielded and thus much colder (Di Francesco et al. 2004; Bergman et al. 2011; Friesen et al. 2014). VLA 1623 A itself is certainly heating up the disk and outflow cavity, evidenced by DCO^+ 5–4 emission on the disk and the presence of c$-C_3H_2$ and C_2H, but on much smaller scales (<100 AU) than in IRAS 16293 because of its lower luminosity.

5.2. Comparison with starless cores and low-mass protostars

In this section, IRAS 16293 and VLA 1623 are placed in the big picture of star formation. For this reason, the two systems described in the previous section are compared with observations of starless cores, embedded low-mass protostars and disks found in the literature. In addition, the multiplicity of the systems is also taken into consideration.

The starless core L1544 exhibits c$-C_3H_2$ close to the dense cloud core center and away from cold regions traced by DCO^+ (Spezzano et al. 2016a,b). This points to an anti-correlation between the chemistry traced by DCO^+ and that by c$-C_3H_2$, which is present in both IRAS 16293 and VLA 1623. In the system NGC1333 IRAS4, C_2H is observed to peak on-source toward each component, including the starless core IRAS4C, which has the strongest emission (Koumpia et al. 2016, 2017). In the young embedded object IRAS15398, C_2H traces the red- and blue-shifted outflow cavity (Jørgensen et al. 2013). In contrast, L1527 presents both C_2H and c$-C_3H_2$ in the envelope and disk component, with enhancements at the centrifugal barrier (Sakai et al. 2010, 2014a, 2016), but no emission along the outflow cavity. The spatial distribution of C_2H and c$-C_3H_2$ is similar in L1527, with the emission from c$-C_3H_2$ being more compact than that of C_2H. In Oph-IRS67, C_2H and c$-C_3H_2$ exist in the same region, although the spatial extent is not the same (Artur de la Villarmois et al. 2018). In the protoplanetary disk TW Hya, C_2H and c$-C_3H_2$ are found to reside in the disk, bordering the millimeter dust, with both molecules showing an identical spatial distribution (Bergin et al. 2016). The c$-C_3H_2$ and C_2H distribution toward VLA 1623 is consistent with that observed in other protostellar systems; however, for IRAS 16293 the lack of correlation between the two molecules is still a puzzle, since no other low-mass protostar or starless core reported in the literature at present presents this situation.

In NGC1333 SVS13, N_2H^+ is detected around 2 of the 4 components of the system (Chen et al. 2009). From the system, SVS13B and SVS13C are Class 0 protostars, but the first has N_2H^+ emission while the second does not. Thus, the uneven distribution of material is not related to the evolutionary stage, but instead is most likely related to the varying envelope temperature.

Several of the systems mentioned above are multiple protostars, as are IRAS 16293 and VLA 1623. The chemical structure is found to not be homogeneous among the individual components of these systems. This would suggest that the components of wide multiple protostellar systems have no effect on the chemistry of each other. For close multiple protostellar systems, the only case shown here is that of VLA1623 A and B, which have a separation of ~200 AU (based on the disk radius of VLA1623 A and a lack of disturbance of the disk by VLA1623 B) and show different chemical structures. However, these are only two cases, and more observations of multiple protostellar systems are needed to further understand the effect of companions on chemical structure.

5.3. Comparison with diffuse clouds, PDRs and intermediate to high-mass protostars

Looking to compare what structures are common throughout the interstellar medium, we compare the distributions found in IRAS 16293 and VLA 1623 with diffuse clouds and PDRs. Furthermore, given that IRAS 16293 is much warmer than VLA 1623, it is also compared to high-mass protostars.

Towards the Horsehead nebula PDR, DCO^+ is observed far from the irradiated edge of the region, with no emission at the edge (Guzmán et al. 2015). The spatial anti-correlation between DCO^+ and $c{-}C_3H_2$ or C_2H suggests a temperature effect, as found for IRAS 16293 and VLA 1623, highlighting that DCO^+ is a really good tracer of cold regions.

$c{-}C_3H_2$ and C_2H show close correlation in spatial distribution towards a number of PDRs, including the Orion Bar (Pety et al. 2007; van der Wiel et al. 2009; Nagy et al. 2015) and the Horsehead Nebula (Cuadrado et al. 2015; Guzmán et al. 2015), with both molecular species sitting at the irradiated, and thus warmer, edge of the region. In addition, a tight correlation between $c{-}C_3H_2$ and C_2H in diffuse clouds has been found (Lucas & Liszt 2000; Gerin et al. 2011; Liszt et al. 2012). The column density $c{-}C_3H_2/C_2H$ ratios calculated toward IRAS 16293 in the center and north positions ($c{-}C_3H_2/C_2H \leq 0.035$) reflect the values found for diffuse clouds ($c{-}C_3H_2/C_2H = 0.048$; Lucas & Liszt 2000; Liszt et al. 2012) and the envelope of L1527 ($c{-}C_3H_2/C_2H = 0.035 - 0.06$; Sakai et al. 2014a).

In high-mass star-forming regions, $c{-}C_3H_2$ and C_2H tend to be strongly correlated, with both lines presenting similar spatial distributions (Pilleri et al. 2013; Mookerjea et al. 2012, 2014). In contrast, toward IRAS 20343+4129, $c{-}C_3H_2$ and C_2H show an anti-correlation around the outflow cavity walls of IRS 1 (Fontani et al. 2012) but not around the UC HII-region of IRS 3. The anti-correlation is explained to possibly be product of the gas density, with an enhancement of C_2H located in the regions with denser gas. Thus, the warmer envelope of IRAS 16293 does not provide a solution to the puzzle of why $c{-}C_3H_2$ and C_2H are anti-correlated in this system, but the difference in density, possibly caused by the outflow direction shift, might provide a possible explanation for the anti-correlation of the two molecules. Chemical processes could also be playng a role in the anti-correlation of $c{-}C_3H_2$ and C_2H toward IRAS 16293.

6. Conclusions

In this work, we present ALMA, SMA and APEX observations of DCO^+, $c{-}C_3H_2$, C_2H, N_2H^+ and N_2D^+ towards IRAS 16293-2422 and VLA 1623-2417, both multiple protostellar systems in ρ Ophiuchus. The spatial distribution of each molecule is compared for both systems. DCO^+ is studied using a simple analytic chemical network coupled with radiative transfer modelling, detailed in Murillo et al. (2015), in order to determine the conditions leading to the observed peak position. Non-LTE molecular excitation and radiative transfer modelling of the observed line brightness temperature ratios is done to derive physical parameters of the regions being traced by the molecules. Finally, the observations and results of VLA 1623-2417 and IRAS 16293-2422 are compared, both between the two sources and other objects, ranging from low- to high-mass protostars, diffuse clouds and PDRs, in order to understand what structures are common.

From this work, we extract the following key points:

1. Temperature is a controlling factor of the chemical structure of a protostellar system. Disks can alter the temperature of the envelope, while UV heating can encourage the start of chemical processes in the outflow cavity.
2. An asymmetric DCO^+ structure is a good tell-tale sign for the presence of a disk, since a disk shadows the envelope at its edge, lowering the temperature and causing DCO^+ to move inwards only along the disk plane.
3. $c{-}C_3H_2$ traces the outflow cavity of IRAS 16293-2422 and VLA 1623-2417, but shows no disk component for either source.
4. Despite both VLA 1623-2417 and IRAS 16293-2422 being low-mass Class 0 embedded objects, their structure and chemical richness varies considerably, with VLA 1623-2417 being line poor. Its much lower luminosity, and consequently lower temperatures, coupled with a large cold disk, are likely at the root of this difference.

Although only two sources are studied in this work and some results in the literature, there is evidence pointing to a lack of correlation between multiplicity and the chemical structure of the envelope of these systems, at least in the embedded phase. Nevertheless, multiple systems do provide an interesting way to compare the structure with similar conditions. It would be possible, however, that the heating from companion sources would affect the chemistry as the envelope clears. Further comparison of embedded multiple protostellar systems is needed to confirm these results.

Acknowledgements. The authors thank O. Sipilä, P. Caselli, S. Spezzano, N. Sakai and C. Favre for helpful discussions on chemistry. We are grateful to the APEX staff for support with the observations of VLA1623. This paper made use of the following ALMA data: ADS/JAO.ALMA 2011.0.00902.S, 2013.1.01004.S and 2013.1.00278.S. ALMA is a partnership of ESO (representing its member states), NSF (USA), and NINS (Japan), together with NRC (Canada) and NSC and ASIAA (Taiwan), in cooperation with the Republic of Chile. The Joint ALMA Observatory is operated by ESO, AUI/NRAO, and NAOJ. The 2011.0.00902.S data was obtained by N.M.M. while she was a Master student at National Tsing Hua University, Taiwan, under the supervision of S.P.L. Astrochemistry in Leiden is supported by the European Union A-ERC grant 291141 CHEMPLAN, by the Netherlands Research School for Astronomy (NOVA), by a Royal Netherlands Academy of Arts and Sciences (KNAW) professor prize. The group of JKJ acknowledges support from the European Research Council (ERC) under the European Union's Horizon 2020 research and innovation programme (grant agreement No 646908) through ERC Consolidator Grant "S4F". Research at Centre for Star and Planet Formation is funded by the Danish National Research Foundation. MND acknowledges the financial support of the Center for Space and Habitability (CSH) Fellowship and the IAU Gruber Foundation Fellowship.

References

Aikawa, Y. & Herbst, E. 1999, A&A, 351, 233
Aikawa, Y., Umebayashi, T., Nakano, T., & Miyama, S. M. 1999, ApJ, 519, 705
Aikawa, Y., Wakelam, V., Hersant, F., Garrod, R. T., & Herbst, E. 2012, ApJ, 760, 40
Anderl, S., Maret, S., Cabrit, S., et al. 2016, A&A, 591, A3
André, P., Belloche, A., Motte, F., & Peretto, N. 2007, A&A, 472, 519
André, P., Martin-Pintado, J., Despois, D., & Montmerle, T. 1990, A&A, 236, 180
Artur de la Villarmois, E., Kristensen, L. E., Jørgensen, J. K., et al. 2018, ArXiv e-prints [arXiv:1802.09286]
Bacmann, A., Taquet, V., Faure, A., Kahane, C., & Ceccarelli, C. 2012, A&A, 541, L12
Belitsky, V., Lapkin, I., Monje, R., et al. 2006, in Proc. SPIE, Vol. 6275, Society of Photo-Optical Instrumentation Engineers (SPIE) Conference Series, 62750G
Bergin, E. A., Du, F., Cleeves, L. I., et al. 2016, ApJ, 831, 101
Bergman, P., Parise, B., Liseau, R., & Larsson, B. 2011, A&A, 527, A39
Bergner, J. B., Öberg, K. I., Garrod, R. T., & Graninger, D. M. 2017, ApJ, 841, 120
Bisschop, S. E., Fraser, H. J., Öberg, K. I., van Dishoeck, E. F., & Schlemmer, S. 2006, A&A, 449, 1297
Bisschop, S. E., Jørgensen, J. K., Bourke, T. L., Bottinelli, S., & van Dishoeck, E. F. 2008, A&A, 488, 959
Bogey, M., Demuynck, C., & Destombes, J. L. 1986, Chem. Phys. Lett., 125, 383
Bogey, M., Demuynck, C., Destombes, J. L., & Dubus, H. 1987, J. Mol. Spectrosc., 122, 313
Botschwina, P., Horn, M., Flugge, J., & Seeger, S. 1993, J. Chem. Soc., Faraday Trans., 89, 2219
Bottinelli, S., Ceccarelli, C., Neri, R., et al. 2004, ApJ, 617, L69
Caratti o Garatti, A., Giannini, T., Nisini, B., & Lorenzetti, D. 2006, A&A, 449, 1077
Caselli, P. & Ceccarelli, C. 2012, A&A Rev., 20, 56
Caselli, P. & Dore, L. 2005, A&A, 433, 1145
Cazzoli, G., Cludi, L., Buffa, G., & Puzzarini, C. 2012, ApJS, 203, 11
Chandra, S. & Kegel, W. H. 2000, A&AS, 142, 113
Chen, X., Launhardt, R., & Henning, T. 2009, ApJ, 691, 1729
Codella, C., Cabrit, S., Gueth, F., et al. 2014, A&A, 568, L5
Coutens, A., Jørgensen, J. K., van der Wiel, M. H. D., et al. 2016, A&A, 590, L6
Crapsi, A., Caselli, P., Walmsley, C. M., et al. 2005, ApJ, 619, 379
Crimier, N., Ceccarelli, C., Maret, S., et al. 2010, A&A, 519, A65
Cuadrado, S., Goicoechea, J. R., Pilleri, P., et al. 2015, A&A, 575, A82
Di Francesco, J., André, P., & Myers, P. C. 2004, ApJ, 617, 425
Drozdovskaya, M. N., van Dishoeck, E. F., Jørgensen, J. K., et al. 2018, MNRAS, 476, 4949
Drozdovskaya, M. N., Walsh, C., Visser, R., Harsono, D., & van Dishoeck, E. F. 2014, MNRAS, 445, 913
Drozdovskaya, M. N., Walsh, C., Visser, R., Harsono, D., & van Dishoeck, E. F. 2015, MNRAS, 451, 3836
Dunham, M. M., Stutz, A. M., Allen, L. E., et al. 2014, Protostars and Planets VI, 195
Emprechtinger, M., Caselli, P., Volgenau, N. H., Stutzki, J., & Wiedner, M. C. 2009, A&A, 493, 89
Endres, C. P., Schlemmer, S., Schilke, P., Stutzki, J., & Müller, H. S. P. 2016, J. Mol. Spectrosc., 327, 95
Evans, II, N. J. 1999, ARA&A, 37, 311
Evans, II, N. J., Rawlings, J. M. C., Shirley, Y. L., & Mundy, L. G. 2001, ApJ, 557, 193
Favre, C., Bergin, E. A., Cleeves, L. I., et al. 2015, ApJ, 802, L23
Favre, C., López-Sepulcre, A., Ceccarelli, C., et al. 2017, A&A, 608, A82
Fayolle, E. C., Öberg, K. I., Garrod, R. T., van Dishoeck, E. F., & Bisschop, S. E. 2015, A&A, 576, A45
Flower, D. R. 1999, MNRAS, 305, 651
Flower, D. R., Pineau Des Forêts, G., & Walmsley, C. M. 2006, A&A, 449, 621
Fontani, F., Palau, A., Busquet, G., et al. 2012, MNRAS, 423, 1691
Friesen, R. K., Di Francesco, J., Bourke, T. L., et al. 2014, ApJ, 797, 27
Furuya, K., Aikawa, Y., Tomida, K., et al. 2012, ApJ, 758, 86
Galli, D., Walmsley, M., & Gonçalves, J. 2002, A&A, 394, 275
Garay, G., Mardones, D., Rodríguez, L. F., Caselli, P., & Bourke, T. L. 2002, ApJ, 567, 980
Garrod, R. T. & Herbst, E. 2006, A&A, 457, 927
Gerin, M., Kaźmierczak, M., Jastrzebska, M., et al. 2011, A&A, 525, A116
Girart, J. M., Estalella, R., Palau, A., Torrelles, J. M., & Rao, R. 2014, ApJ, 780, L11
Güsten, R., Nyman, L. Å., Schilke, P., et al. 2006, A&A, 454, L13
Guzmán, V. V., Pety, J., Goicoechea, J. R., et al. 2015, ApJ, 800, L33
Harsono, D., Jørgensen, J. K., van Dishoeck, E. F., et al. 2014, A&A, 562, A77
Herbst, E. & van Dishoeck, E. F. 2009, ARA&A, 47, 427
Hincelin, U., Commerçon, B., Wakelam, V., et al. 2016, ApJ, 822, 12
Hincelin, U., Wakelam, V., Commerçon, B., Hersant, F., & Guilloteau, S. 2013, ApJ, 775, 44
Hogerheijde, M. R. & van der Tak, F. F. S. 2000, A&A, 362, 697
Huang, J., Öberg, K. I., Qi, C., et al. 2017, ApJ, 835, 231
Jacobsen, S. K., Jørgensen, J. K., van der Wiel, M. H. D., et al. 2018, A&A, 612, A72
Jørgensen, J. K., Bourke, T. L., Myers, P. C., et al. 2005a, ApJ, 632, 973
Jørgensen, J. K., Bourke, T. L., Nguyen Luong, Q., & Takakuwa, S. 2011, A&A, 534, A100
Jørgensen, J. K., Schöier, F. L., & van Dishoeck, E. F. 2002, A&A, 389, 908
Jørgensen, J. K., Schöier, F. L., & van Dishoeck, E. F. 2004, A&A, 416, 603
Jørgensen, J. K., Schöier, F. L., & van Dishoeck, E. F. 2005b, A&A, 437, 501
Jørgensen, J. K., Schöier, F. L., & van Dishoeck, E. F. 2005c, A&A, 435, 177
Jørgensen, J. K., van der Wiel, M. H. D., Coutens, A., et al. 2016, A&A, 595, A117
Jørgensen, J. K., Visser, R., Sakai, N., et al. 2013, ApJ, 779, L22
Koumpia, E., Semenov, D. A., van der Tak, F. F. S., Boogert, A. C. A., & Caux, E. 2017, A&A, 603, A88
Koumpia, E., van der Tak, F. F. S., Kwon, W., et al. 2016, A&A, 595, A51
Kristensen, L. E., Klaassen, P. D., Mottram, J. C., Schmalzl, M., & Hogerheijde, M. R. 2013, A&A, 549, L6
Li, Z.-Y., Banerjee, R., Pudritz, R. E., et al. 2014, Protostars and Planets VI, 173
Lindberg, J. E., Charnley, S. B., & Cordiner, M. A. 2016, ApJ, 833, L14
Lindberg, J. E., Charnley, S. B., Jørgensen, J. K., Cordiner, M. A., & Bjerkeli, P. 2017, ApJ, 835, 3
Lindberg, J. E., Jørgensen, J. K., Brinch, C., et al. 2014a, A&A, 566, A74
Lindberg, J. E., Jørgensen, J. K., Green, J. D., et al. 2014b, A&A, 565, A29
Liseau, R., Larsson, B., Brandeker, A., et al. 2003, A&A, 402, L73
Liseau, R., Larsson, B., Lunttila, T., et al. 2015, A&A, 578, A131
Liszt, H., Sonnentrucker, P., Cordiner, M., & Gerin, M. 2012, ApJ, 753, L28
Loinard, L., Torres, R. M., Mioduszewski, A. J., & Rodríguez, L. F. 2008, ApJ, 675, L29
Loinard, L., Zapata, L. A., Rodríguez, L. F., et al. 2013, MNRAS, 430, L10
Lucas, R. & Liszt, H. S. 2000, A&A, 358, 1069
Lykke, J. M., Coutens, A., Jørgensen, J. K., et al. 2017, A&A, 597, A53
Maret, S., Bergin, E. A., & Lada, C. J. 2006, Nature, 442, 425
Mookerjea, B., Hassel, G. E., Gerin, M., et al. 2012, A&A, 546, A75
Mookerjea, B., Vastel, C., Hassel, G. E., et al. 2014, A&A, 566, A61
Müller, H. S. P., Klaus, T., & Winnewisser, G. 2000, A&A, 357, L65
Murillo, N. M., Bruderer, S., van Dishoeck, E. F., et al. 2015, A&A, 579, A114
Murillo, N. M. & Lai, S.-P. 2013, ApJ, 764, L15
Murillo, N. M., Lai, S.-P., Bruderer, S., Harsono, D., & van Dishoeck, E. F. 2013, A&A, 560, A103
Murillo, N. M., van Dishoeck, E. F., Tobin, J. J., & Fedele, D. 2016, A&A, 592, A56
Nagy, Z., Ossenkopf, V., Van der Tak, F. F. S., et al. 2015, A&A, 578, A124
Öberg, K. I., Lauck, T., & Graninger, D. 2014, ApJ, 788, 68
Oya, Y., Sakai, N., López-Sepulcre, A., et al. 2016, ApJ, 824, 88
Padovani, M., Walmsley, C. M., Tafalla, M., Galli, D., & Müller, H. S. P. 2009, A&A, 505, 1199
Pagani, L., Daniel, F., & Dubernet, M.-L. 2009a, A&A, 494, 719
Pagani, L., Vastel, C., Hugo, E., et al. 2009b, A&A, 494, 623
Persson, M. V., Harsono, D., Tobin, J. J., et al. 2016, A&A, 590, A33
Pety, J., Goicoechea, J. R., Hily-Blant, P., Gerin, M., & Teyssier, D. 2007, A&A, 464, L41
Pilleri, P., Treviño-Morales, S., Fuente, A., et al. 2013, A&A, 554, A87
Pineda, J. E., Maury, A. J., Fuller, G. A., et al. 2012, A&A, 544, L7
Punanova, A., Caselli, P., Pon, A., Belloche, A., & André, P. 2016, A&A, 587, A118
Reipurth, B., Clarke, C. J., Boss, A. P., et al. 2014, Protostars and Planets VI, 267
Sakai, N., Oya, Y., López-Sepulcre, A., et al. 2016, ApJ, 820, L34
Sakai, N., Oya, Y., Sakai, T., et al. 2014a, ApJ, 791, L38
Sakai, N., Sakai, T., Hirota, T., et al. 2014b, Nature, 507, 78
Sakai, N., Sakai, T., Hirota, T., & Yamamoto, S. 2010, ApJ, 722, 1633
Sakai, N. & Yamamoto, S. 2013, Chemical Reviews, 113, 8981
Salinas, V. N., Hogerheijde, M. R., Mathews, G. S., et al. 2017, A&A, 606, A125
Santangelo, G., Murillo, N. M., Nisini, B., et al. 2015, A&A, 581, A91
Sastry, K. V. L. N., Helminger, P., Charo, A., Herbst, E., & De Lucia, F. C. 1981, ApJ, 251, L119
Schöier, F. L., Jørgensen, J. K., van Dishoeck, E. F., & Blake, G. A. 2002, A&A, 390, 1001
Schöier, F. L., van der Tak, F. F. S., van Dishoeck, E. F., & Black, J. H. 2005, A&A, 432, 369
Shirley, Y. L. 2015, PASP, 127, 299
Spezzano, S., Bizzocchi, L., Caselli, P., Harju, J., & Brünken, S. 2016a, A&A, 592, L11
Spezzano, S., Gupta, H., Brünken, S., et al. 2016b, A&A, 586, A110
Spezzano, S., Tamassia, F., Thorwirth, S., et al. 2012, ApJS, 200, 1

Stark, R., Sandell, G., Beck, S. C., et al. 2004, ApJ, 608, 341
Tassis, K., Willacy, K., Yorke, H. W., & Turner, N. J. 2012, ApJ, 753, 29
Tobin, J. J., Bergin, E. A., Hartmann, L., et al. 2013, ApJ, 765, 18
Tobin, J. J., Hartmann, L., Chiang, H.-F., et al. 2012, Nature, 492, 83
van der Tak, F. F. S., Black, J. H., Schöier, F. L., Jansen, D. J., & van Dishoeck, E. F. 2007, A&A, 468, 627
van der Wiel, M. H. D., van der Tak, F. F. S., Ossenkopf, V., et al. 2009, A&A, 498, 161
van Dishoeck, E. F., Blake, G. A., Jansen, D. J., & Groesbeck, T. D. 1995, ApJ, 447, 760
van Dishoeck, E. F., Jansen, D. J., & Phillips, T. G. 1993, in , 541–566
van't Hoff, M. L. R., Walsh, C., Kama, M., Facchini, S., & van Dishoeck, E. F. 2017, A&A, 599, A101
Vassilev, V., Meledin, D., Lapkin, I., et al. 2008, A&A, 490, 1157
Visser, R., Doty, S. D., & van Dishoeck, E. F. 2011, A&A, 534, A132
Visser, R., van Dishoeck, E. F., Doty, S. D., & Dullemond, C. P. 2009, A&A, 495, 881
Walmsley, C. M., Flower, D. R., & Pineau des Forêts, G. 2004, A&A, 418, 1035
Willacy, K., Alexander, C., Ali-Dib, M., et al. 2015, Space Sci. Rev., 197, 151
Wootten, A., Andre, P., Despois, D., & Sargent, A. 1994, in Astronomical Society of the Pacific Conference Series, Vol. 65, Clouds, Cores, and Low Mass Stars, ed. D. P. Clemens & R. Barvainis, 294
Yeh, S. C. C., Hirano, N., Bourke, T. L., et al. 2008, ApJ, 675, 454
Yen, H.-W., Koch, P. M., Takakuwa, S., et al. 2017, ApJ, 834, 178
Yoneda, H., Tsukamoto, Y., Furuya, K., & Aikawa, Y. 2016, ApJ, 833, 105
Zapata, L. A., Loinard, L., Rodríguez, L. F., et al. 2013, ApJ, 764, L14

Appendix A: Interferometric Observations

Table A.1 lists details of the interferometric observations used in this work for both systems, IRAS 16293 and VLA 1623. For VLA 1623, the Cycle 2 Band 6 12m array observations have both long (C35-5) and short (C34-1) baselines. The short baselines were observed to bridge the baseline ranges between the ACA and 12m observations. The c−C_3H_2 observations toward VLA 1623 presented in this work was detected with the 12m array short baselines but not the long baselines, suggesting that the emission arises from regions larger than ∼0.5″.

Appendix B: Additional c−C_3H_2 and C_2H spectra

The spectra for all transitions of c−C_3H_2 and C_2H toward the south, center and north positions of IRAS 16293 are shown in Fig. B.1. The systemic velocity of IRAS 16293 A and B are marked on the spectra with dashed lines. The anti-correlation of the two molecules is evident from the spectra, as well as a slight velocity shift in C_2H between the center and north positions.

Appendix C: Peak intensities and line ratios

The observed peak intensities of C_2H and c−C_3H_2 are listed in this appendix (Table C.1). The peak intensities are used in Sect. 4.2 and 4.3. In addition, the detailed calculation of expected peak intensities for N_2H^+ and N_2D^+ are also summarized here (Table C.2).

Single-dish observations of low-J transitions of CN, HCN and HNC show strong detections relative to other embedded systems (Jørgensen et al. 2004). Our recent APEX observations also detected NO towards VLA 1623. However, single-dish observations of NH_3 (Wootten et al. 1994; Liseau et al. 2003) and N_2H^+ (Liseau et al. 2015; Punanova et al. 2016) indicate that these molecules have very low abundances at the position of VLA 1623. N_2D^+ also exhibits the same behaviour (Punanova et al. 2016). Furthermore, *Herschel* observations of high-J N_2H^+ towards VLA 1623 (Liseau et al. 2015; Favre et al. 2017) show that the molecule is detected up to the J = 6–5 transition peaking at ∼0.1 K km s^{-1} but the emission is extended. The observed parameters of N_2H^+ and N_2D^+ from Punanova et al. (2016) and Favre et al. (2017) are listed in Table C.2.

Using the observed transitions of N_2H^+ and N_2D^+, we derive density and excitation temperature with the method described in Sect. 4.1. The different beam sizes of the observations require a beam dilution correction factor that is given by $T'_{\rm mb} = T_{\rm mb,obs} \frac{\Omega_{\rm beam}}{\Omega_{\rm source}}$, where $T'_{\rm mb}$ and $T_{\rm mb,obs}$ are the corrected and observed main beam temperature, respectively, $\Omega_{\rm beam}$ is the solid angle of the single-dish beam and $\Omega_{\rm source}$ is the solid angle subtended by the source. We assume the emission is concentrated in the region of the smaller beam, which would be of 26.5″ for N_2H^+ and 16.3″ for N_2D^+.

To compare with our ALMA observations, the expected peak for N_2H^+ 4–3 and N_2D^+ 3–2 is derived from the observations of Punanova et al. (2016) and Favre et al. (2017). The N_2H^+ molecular data file without hyperfine structure is used to calculate the kinetic temperature of both molecules. The collisional rate coefficients for N_2H^+ are taken to be the same as HCO^+ (Botschwina et al. 1993) and extrapolated (Schöier et al. 2005). Since LAMDA does not have a molecular data file for N_2D^+, the data file for N_2H^+ is used, selecting the corresponding transition rather than frequency. For the predicted peak emissions for N_2H^+ 4–3 and N_2D^+ 3–2, two cases are examined: i) the observed emission is evenly distributed in the single-dish beam (i.e., beam filling factor = 1) and ii) the emission is concentrated in a 1″ region (i.e. beam filling factor < 1). The second case introduces a beam dilution correction. The results of the calculation are listed in Table C.2.

The kinetic temperature and number density obtained in our calculations (∼11 K, ∼10^{7-9} cm^{-3}) are slightly higher than those previously reported (7.7 K, 10^6 cm^{-3}; Punanova et al. 2016). The column densities, however, are similar to those reported in Punanova et al. (2016). For N_2H^+, our results are also consistent with those reported in Liseau et al. (2015).

Using the physical parameters obtained from the DCO^+ 5–4/3–2 ratio (Sect. 4.1 and Table 4), we calculate a column density of 1.5–2×10^{13} cm^{-2} for N_2D^+. If instead we use the physical parameters obtained from the N_2D^+ observations towards VLA 1623, we find a column density of 4–5×10^{13} cm^{-2} for N_2D^+ 3–2 towards IRAS 16293. For both sets of parameters, the column density is higher by one order of magnitude in comparison to the N_2D^+ toward VLA 1623.

Appendix D: PILS full spectra

The PILS survey spectra (Jørgensen et al. 2016) is reproduced here for the south c−C_3H_2 peak position and at one beam away from the position of IRAS 16293 B . Figures D.1, D.2 and D.3 present the full spectra for both positions. At the south c−C_3H_2 peak position, the spectra is multiplied by a factor of 10 to bring out the features. Few molecular lines are detected at this position, apart from common molecules like HCO^+ and CO, only c−C_3H_2 and H_2CS are detected.

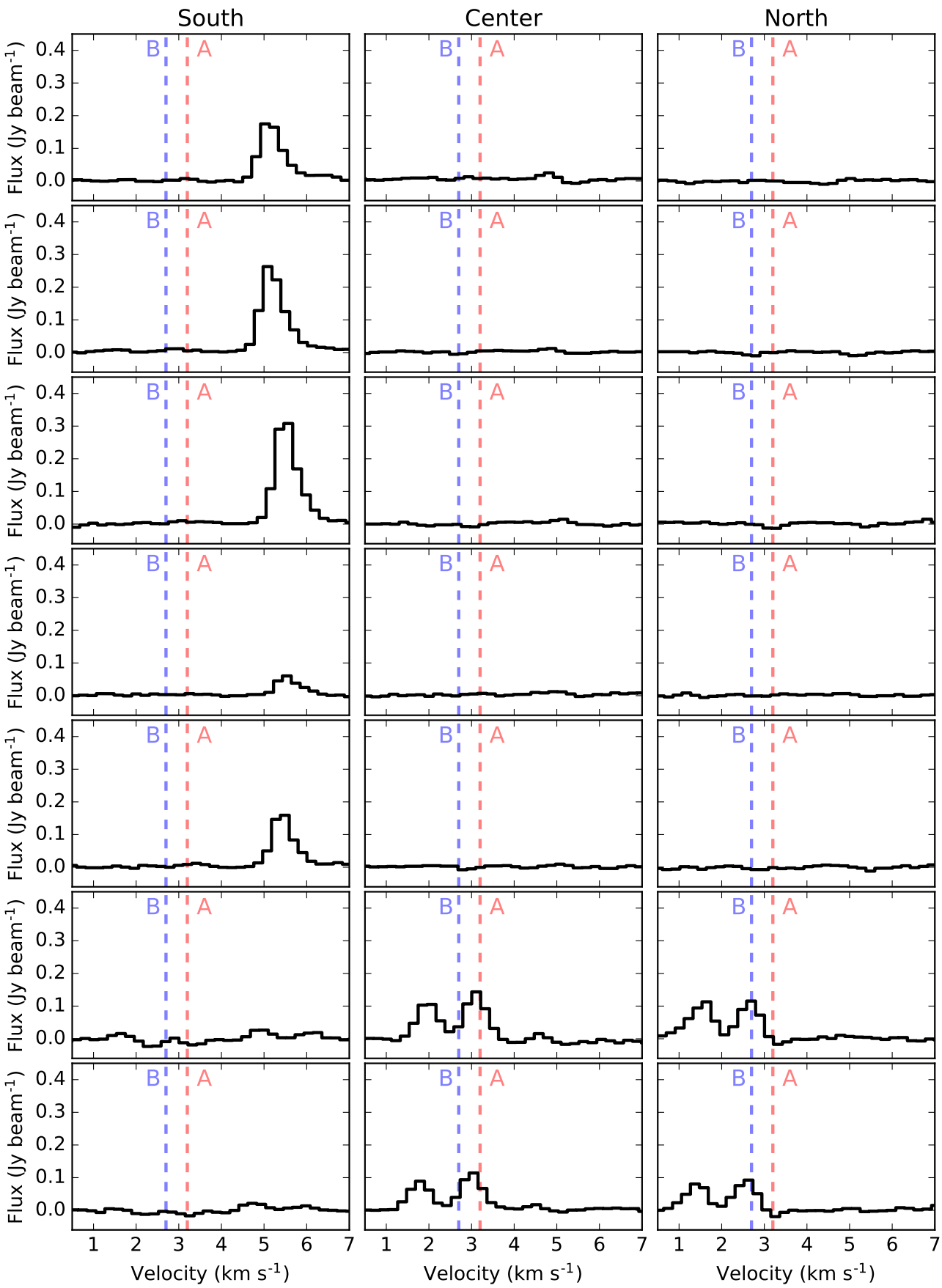

Fig. B.1. IRAS 16293-2422 ALMA spectra for all transitions of c−C_3H_2 and C_2H for each of the south, center and north positions shown in Fig. 4. The systemic velocities of sources A and B are marked with the vertical dashed lines. The anti-correlation of c−C_3H_2 and C_2H is also evident in the spectra shown here.

Table A.1. Interferometric observations

Dataset	Frequency GHz	UV-baseline range kλ	Beam $''$	Largest scale $''$	Field of View $''$	Noise mJy beam^{-1}
IRAS 16293-2422						
Combined 12m+ACA	329.1 – 362.8	10 ~ 352	0.5×0.5	13	19.5	7–10
ACA	329.1 – 362.8	10 ~ 60	5.25×2.36	13	60	440
SMA Compact	215.6–227.6	6 ~ 91	5.5×3.2	20	64	240
VLA 1623-2217						
Cycle 0 12m	216.4 – 232.2	25 ~ 310	0.85×0.56	2.5	28	4–8
Cycle 2 Band 6 12m C35-5	215.5 – 221.4	18 ~ 791	0.45×0.25	1.9	28	7–9
Cycle 2 Band 6 12m C34-1	215.5 – 221.4	11 ~ 253	1.6×0.88	5.3	28	20
Cycle 2 Band 7 12m	359.0 – 372.7	18 ~ 420	0.87×0.54	3.1	17.2	26-95

Table C.1. c$-C_3H_2$ and C_2H peak intensities.

Molecules	c$-C_3H_2$					C_2H			
Transition	5–4	9–8	10–9	$8_{2,6}$–$7_{3,5}$	$8_{3,6}$–$7_{2.5}$	J=9/2–7/2 F=5–4	J=9/2–7/2 F=4–3	J=7/2–5/2 F=4–3	J=7/2–5/2 F=3–
IRAS 16293-2422 (rms = 10 mJy beam^{-1})									
South[a]	240	410	350	90	200	30	30	30	30
Centre[a]	30	30	30	30	30	170	140	140	110
North[a]	30	30	30	30	30	150	130	110	110
VLA 1623-2417 - APEX (rms = 80 mK)									
A	...	...	...	...	...	960	616	680	342

Notes. [(a)] For the positions with non-detections, 3 times the rms noise is used for the calculations.

Table C.2. N_2H^+ and N_2D^+ parameters for VLA 1623-2417.

	Observed			
Parameter	N_2H^+ 1–0[a]	N_2H^+ 6–5[b]	N_2D^+ 1–0[a]	N_2D^+ 2–1[a]
T_{mb} (K)	3.3 ± 0.1	0.2 ± 0.1	0.57 ± 0.1	1.5 ± 0.2
$\Delta v_{\text{single dish}}$ (km s^{-1})	0.56 ± 0.005	0.7 ± 0.2	0.55 ± 0.032	0.55 ± 0.009
η_{mb}	0.95	0.63	0.95	0.94
Ω_{beam} ($''$)	26.5	36	32.1	16.3
Ratio	0.06 ± 0.03		2.6 ± 0.6	
Column density (cm^{-2})	1.3×10^{13}		1.8×10^{12}	
H_2 density (cm^{-3})	$5\times10^7 - 7\times10^9$		$5\times10^7 - 7\times10^9$	
T_{ex} (K)	11 – 12		11 – 12	
$\Omega_{\text{source}} = \Omega_{\text{beam}}$	N_2H^+ 4–3		N_2D^+ 3–2	
$I_{\nu,\text{predicted}}$ (mJy beam^{-1})	99		22	
$\Omega_{\text{beam,obs}}$ ($''$)	0.85		0.76	
σ_{obs} (mJy beam^{-1})	94.9		8.58	
S/N	1		2.6	
$\Omega_{\text{source}} = 1''$	N_2H^+ 4–3		N_2D^+ 3–2	
$I_{\nu,\text{predicted}}$ (mJy beam^{-1})	2631		364	
$\Omega_{\text{beam,obs}}$ ($''$)	0.85		0.76	
σ_{obs} (mJy beam^{-1})	94.9		8.58	
S/N	27		42	

Notes. [(a)] IRAM 30m observations from Punanova et al. (2016). [(b)] *Herschel* observations from Favre et al. (2017)

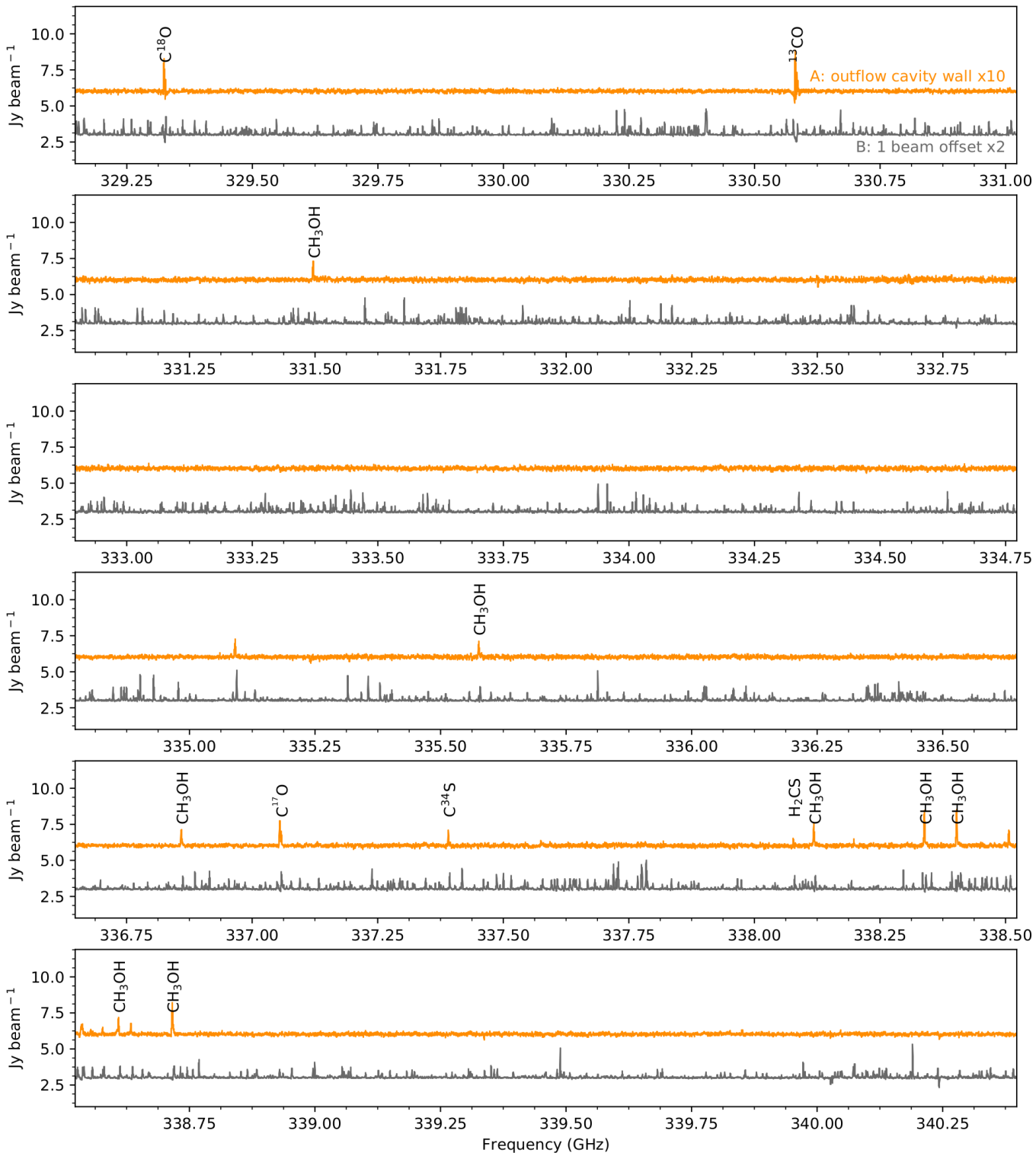

Fig. D.1. Full spectra obtained in the PILS survey for IRAS 16293-2422. Here the frequency range 329.15 to 340.4 GHz is shown. The rest of the spectra is shown in Fig. D.2 and D.3. The spectra for the IRAS 16293-2422 B is one beam away from the source position (α_{J2000} = 16:32:22.581, δ_{J2000} = -24:28:32.80), note that it is multiplied by a factor of 2. The spectra for IRAS 16293-2422 A's outflow cavity wall is centered at the observed peak of c−C_3H_2 (α_{J2000} = 16:32:22.867, δ_{J2000} = -24:28:39.60), note that it is multiplied by a factor of 10 and shows very little emission other than c−C_3H_2, CH_3OH, H_2CS, H_2CO and HCO^+.

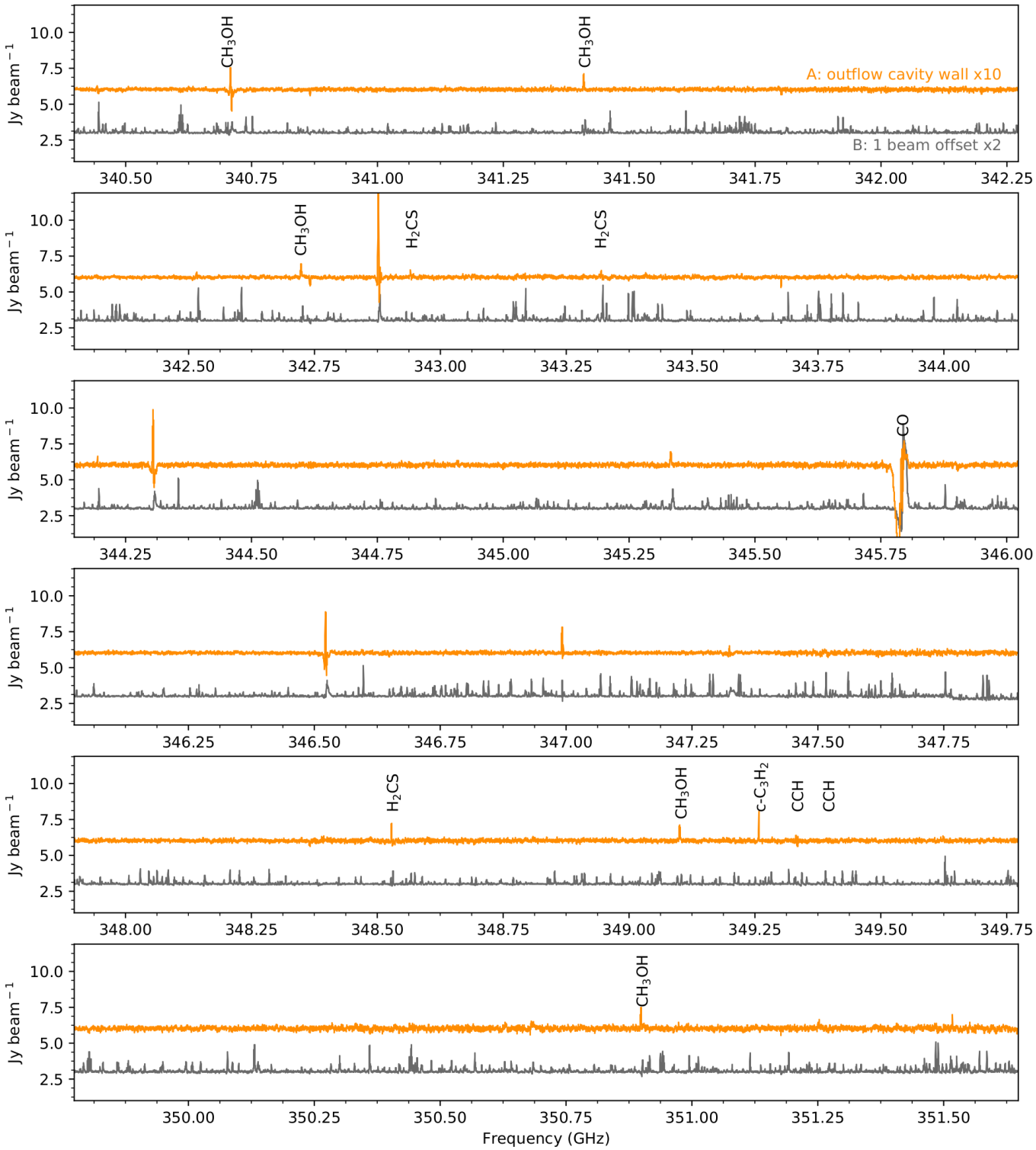

Fig. D.2. Same as in Fig. D.1 but for the frequency range 340.4 to 351.65 GHz. C_2H is marked for reference.

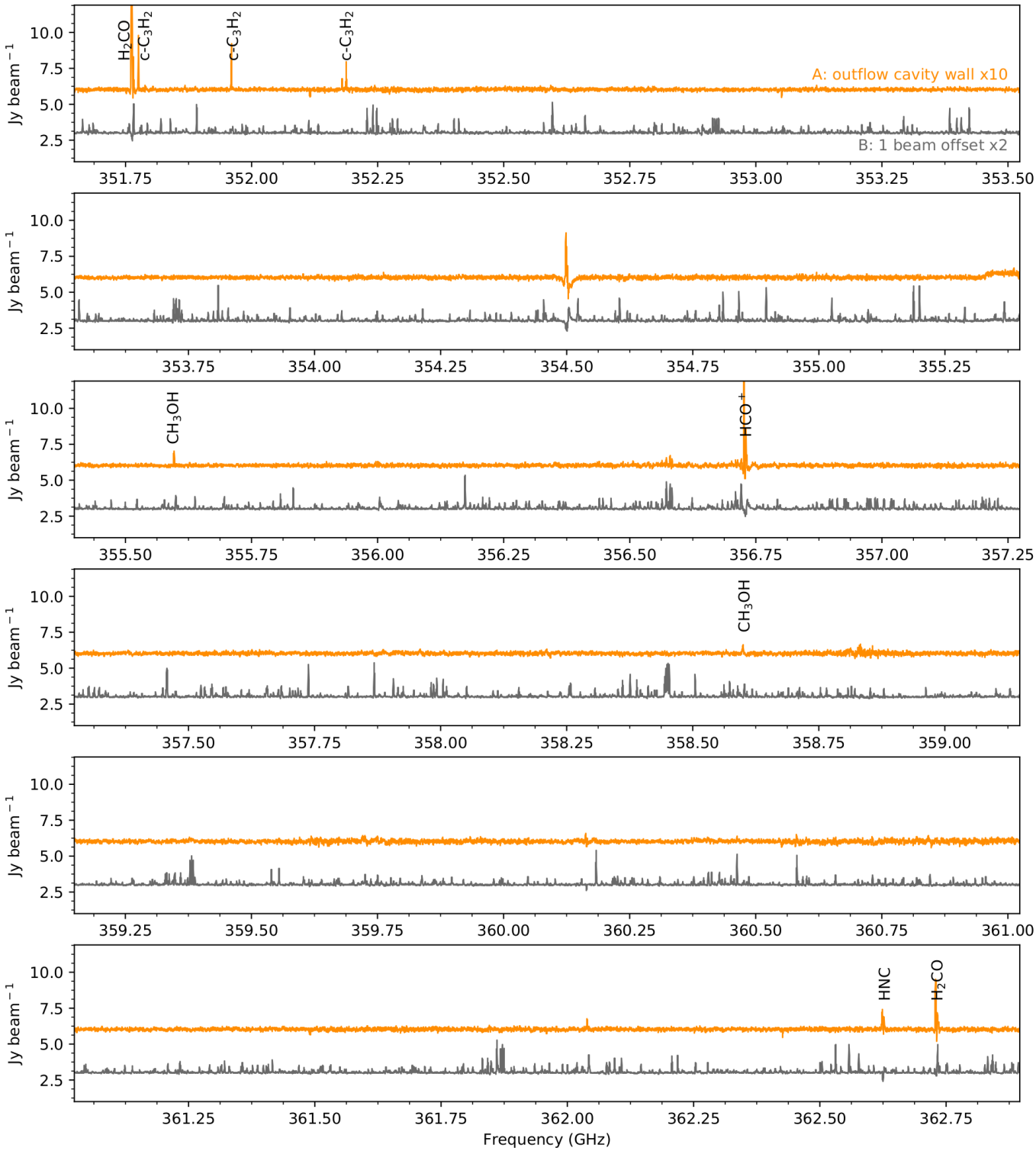

Fig. D.3. Same as in Fig. D.1 but for the frequency range 351.65 to 362.9 GHz.